2018년 8월
석사학위 논문

# Surface Characteristics and Biocompatibility of PEO-treated Ti-40Ta-xZr Alloy in Electrolytes Containing Ca, P, Mg, and Zn Ions

조선대학교 대학원

치의생명공학과

유 지 민

2018년 8월 석사학위 논문
Surface Characteristics and Biocompatibility of PEO-treated Ti-40Ta-xZr Alloy in Electrolytes Containing Ca, P, Mg, and Zn Ions
유 지 민

# Surface Characteristics and Biocompatibility of PEO-treated Ti-40Ta-xZr Alloy in Electrolytes Containing Ca, P, Mg, and Zn Ions

Ca, P, Mg, 및 Zn 이온이 함유된 전해액에서 PEO 처리된 Ti-40Ta-xZr 합금의 표면특성과 생체적합성

2018년 8월 24일

조선대학교 대학원

치의생명공학과

유 지 민

# Surface Characteristics and Biocompatibility of PEO-treated Ti-40Ta-xZr Alloy in Electrolytes Containing Ca, P, Mg, and Zn Ions

지도교수 최 한 철

이 논문을 공학석사학위신청 논문으로 제출함

2018년 04월

조선대학교 대학원

치의생명공학과

유 지 민

# 유지민의 석사학위논문을 인준함

위 원 장 조선대학교 교 수 안 상 건 (인)

위 원 조선대학교 교 수 손 미 경 (인)

위 원 조선대학교 교 수 최 한 철 (인)

2018년 05월

조 선 대 학 교 대 학 원

# CONTENTS

# LIST OF TABLES

# LIST OF FIGURES

# 국 문 초 록

## Ca, P, Mg, 및 Zn 이온이 함유된 전해액에서 PEO 처리된 Ti-40Ta-xZr 합금의 표면특성 및 생체적합성

유 지 민
지도교수 : 최 한 철, 공학/치의학 박사
치의생명공학과
조선대학교 대학원

본 연구에서는 티타늄 합금 (Ti-6Al-4V)의 생체적합성 및 표면특성을 개선하기 위하여 탄탈륨(Ta), 지르코늄(Zr) 등의 원소를 첨가하여 새로운 티타늄 합금을 제조 한 후, 합금의 표면에 플라즈마 전해 산화법(PEO)을 이용하여 Hydroxyapatite (HA)와 같은 세라믹 코팅을 형성시킨 후, 합금의 생체적합성과 표면특성을 연구하였다.

Ti-40Ta-xZr 삼원계 합금은 Ti-40Ta 합금을 기본으로 하여 Zr의 함량을 0, 3, 7, 및 15 wt. %의 함량으로 하여 제조하였다. Ti-40Ta-xZr 합금은 Ar 가스분위기와 1050 ℃에서 1시간 동안 균질화 시킨 다음 얼음물에서 급냉 시켰다. 또한 전기화학적 산화 피막은 0.15 M의 calcium acetate monohydrate + 0.02 M의 calcium glycerophosphate 전해질에서 DC 280V, 3분간 직류전원공급장치를 이용하여 인가하였다. 또한 생체활성을 높이기 위해 전해질에 기능성 물질인 0.0075M의 zinc acetate와 magnesium acetate를 소량 첨가하였다. Ti-40Ta-xZr 합금의 코팅된 표면의 기계적인 특성은 비커스경도와 거칠기테스트, 나노인덴테이션 시험을 통하여 탄성계수를 측정하였으며, 코팅표면의 접촉각을 측정하여 표면 젖음성 (wettability test)을 평가하였고, AFM과 표면거칠기 측정장치를을 이용하여 표면의 거칠기를 측정하였다. 또한, 세포의 활성 및 분화는 HEK 293 cell culture 실험을 통하여 세포증식을 알아보았다. 합금의 표면 특성은 주사전자현미경, EDS, XRF, 그리고 X선 회절분석을 사용하여 분석하였으며 다음과 같은 결과를 얻었다.

1. Ti-40Ta-xZr 합금의 조직은 Zr의 함량이 증가할수록 침상구조(needle-like)에서 β상의 등축정 구조가 나타났고, XRD 분석 결과에서도 β상의 피크가 증가하는 양상이 보였다.
2. 플라즈마 전해 산화방법(PEO)을 이용하여 표면에 다공성의 거친 생체활성물질인 HA로 코팅 시킨 결과, Zr의 함량이 증가함에 따라 표면에 형성된 마이크로 포어의 크기가 증가하였으며, 표면뿐만 아니라 포어의 내부에서 2차 포어가 형성됨이 관찰되었다. 또한 표면에서는 $TiO_2$, $Ta_2O_5$, $ZrO_2$ 와 같은 산화피막이 형성되었다.
3. PEO 처리한 표면에서 각 원소들이 잘 분포되었으며 또한 특정 원소들이 포어 안보다 밖에서 분포가 더 잘 이루어지는 것을 EDS line profile 분석을 통해 확인하였다. EDS분석 결과로 얻은 Ca/P 비율은 Zr의 함량이 증가할수록 증가하였다.
4. PEO처리한 Ti-40Ta-xZr합금의 표면의 거칠기와 비커스경도, 탄성계수는 Zr 함량이 증가함에 따라 감소하였다.
5. HA코팅 된 Ti-40Ta-xZr 합금의 젖음성은 PEO처리한 시편에서 높은 젖음성이 나타났으며, Zr의 함량이 증가할수록 낮은 접촉각이 나타났다. 또한 Ca, P에 Mg과 Zn 이온을 도핑하여 HA 코팅한 경우에는 접촉각이 감소하는 경향을 보였다.

결론적으로 Ti-40Ta-xZr 합금의 표면 변형은 다공성의 표면 구조로 인해 넓은 표면적을 형성하고, 생체에 적합한 기능성 물질을 도핑 함으로써 생체적합성을 향상시키며, 또한 피막의 $ZrO_2$의 산화물은 막의 습윤성을 향상시키므로 뛰어난 표면 개질을 보임을 알 수 있었다.

# Ⅰ. INTRODUCTION

Pure titanium and titanium alloys have been regarded as a replacement for damaged bones and joints due to their excellent strength, fracture toughness, high corrosion resistance, and biocompatibility. However, the Ti-6Al-4V alloy has a high modulus of elasticity (110 GPa) when compared to the cortical bone (10-30 GPa). In addition, toxic elements, which are harmful to vanadium and aluminum elements, also cause concern. For this reason, transition metals such as Mo, Ta, Zr, Nb, and Sn, which are nontoxic alloying elements for the stabilization of the volume center β phase, have been studied as materials of the new titanium alloys[1]. The low elastic modulus and high strength are likely to allow the bone tissue to grow in a stable $TiO_2$ layer, that is, to achieve good osseointegration. Nb and Ta are among the most effective titanium β-stabilizers and have been shown to reduce the modulus of elasticity, and addition of a small amount of Zr improves the corrosion resistance, biocompatibility and blood compatibility when alloyed with Ti by the action of $ZrO_2$ layer on the surface[2-5]. Ti, Ta, and Zr belong to the same series in the periodic table, and it is assumed that adding Zr to the Ti-Ta alloy will have excellent mechanical properties and biocompatibility.

Various surface modification methods have been introduced to improve the biocompatibility and adhesion of the alloys produced. A variety of techniques have been developed to improve the chemical and biological properties of coatings on surfaces such as sol-gel technology, SBF (simulated body fluid) immersion, chemical treatment, plasma spraying, hydrothermal treatment, anodization and micro-arc oxidation (MAO)[6].

Plasma electrolytic oxidation (PEO), also known as MAO or spark plasma anodization, which combines high pressure spark and electrochemical oxidation, is unique in that it forms a solid and relatively thick ceramic oxide film in light metals such as Zr, Al, Mg and, Ti. It has attracted attention as a relatively convenient method. The coatings produced by the PEO process are not

only porous, they are evenly coated on the alloy and have good adhesion to the substrate[6-7].

Ceramics, which are PEO coating materials, are based on hydroxyapatite (HA) and calcium phosphate. HA ($Ca_{10}(PO_4)_6(OH)_2$) is a very promising ceramic material with excellent bioactivity and compatibility due to its excellent similarity with bone mineral components in chemical and structural aspects[8-9]. The HA coating was attracted to the surface when the pulses were applied at high cathodic current and $OH^-$ and $PO_4^{3-}$ ions caused electrochemical deposition of HA after the reaction[10]. The general formula for HA is $M_{10}(XO_4)_6Y_2$. M is generally a divalent cation such as $Ca^{2+}$, $Sr^{2+}$, $Ba^{2+}$, $Cd^{2+}$, $Pb^{2+}$, monovalent and trivalent cations such as $Na^+$, $K^+$ and $Al^{3+}$, and $XO_4$ is generally $PO_4^{3-}$, $VO_4^{3-}$ or $AsO_4^{3-}$. Finally, Y is $OH^-$, $F^-$, $Cl^-$, $Br^-$, which are monovalent anions[11-12].

Functional materials, magnesium (Mg) and zinc (Zn) were used in the HA doping process to improve HA properties in place of hydroxyapatite. Mg and Zn ions were added to change the composition of the Ca, P solution. The doping of ions in HA plays an important role in the biological response of bone cells, as well as changing the spatial grouping of crystal structure, morphology, thermal stability and mechanical properties[13]. Mg is closely related to the calcification of calcified tissue and indirectly affects mineral metabolism. Deficiency of Mg affects not only mechanical properties but also skeletal metabolism such as stopping bone growth and reducing osteoclast activity. Zn deficiency has also been reported to reduce bone mineral density and ductility, increasing the likelihood of fracture. The use of Mg and Zn as an alternative element has been shown to promote osteoblast activity, and the replacement of these divalent ions may improve the bioactivity of HA[13-16].

Therefore, these researches have been focused on HA precipitation and substituted HA with Ca, P, Mg, and Zn for improvement of biocompatibility.

In this study, the surface characteristics and biocompatibility of PEO-treated Ti-40Ta-xZr alloys in electrolytes containing Ca, P, Mg, and Zn ions have evaluated using various experiments. After surface coating, various experiments such as surface roughness test, wettability test, cell adhesion,

and proliferation were conducted to investigate biocompatibility of surface films. Surface characteristics were analyzed by FE-SEM, EDS, and XRD.

# Ⅱ. BACKGROUND

## Ⅱ. 1. Characteristics of bio-metallic materials[17)]

There are a number of characteristics that must be borne in selecting or developing bio alloys. The characteristics of the medical metal material are as follows: the binding property of the initial bone fiber cells to the metal, the corrosion resistance in the living body atmosphere, the reactivity with the corrosion products between the bone fiber cells, biological fluids, and blood. The properties as a metallic bio-materials are determined by the bond between the initial bone fiber cell and metal, also, the corrosion resistance in the biological atmosphere, the reactivity of corrosion product, bone fiber cell, biological fluid, blood, and the enzyme.

Fig. 1 shows the results of a study on the cytotoxicity of metal oxide and metal ions and bone-fiber cells formed around the implant when metal elements were implanted in bone tissue. Fe, Co, Bi, Ag, Sr, Mg, V, Cu, Zn, Cd, and Hg are highly cytotoxic elements. Zr, Nb, Ta, Pt, and Ti have been shown to be excellent in biocompatibility.

Fig. 2 shows the results of investigating the polarization resistance and biocompatibility of metal elements. Zr, Ti, Nb, Ta, and Pt were determined to be metal elements having excellent biocompatibility according to degree of polarization resistance.

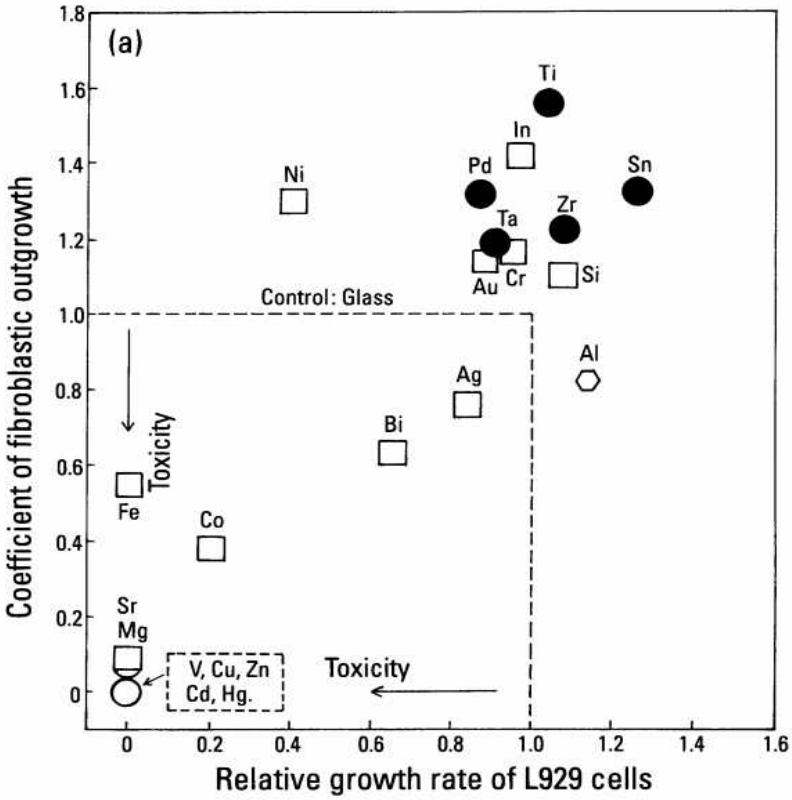


Fig. 1. The cytotoxicity of metal elements[17].

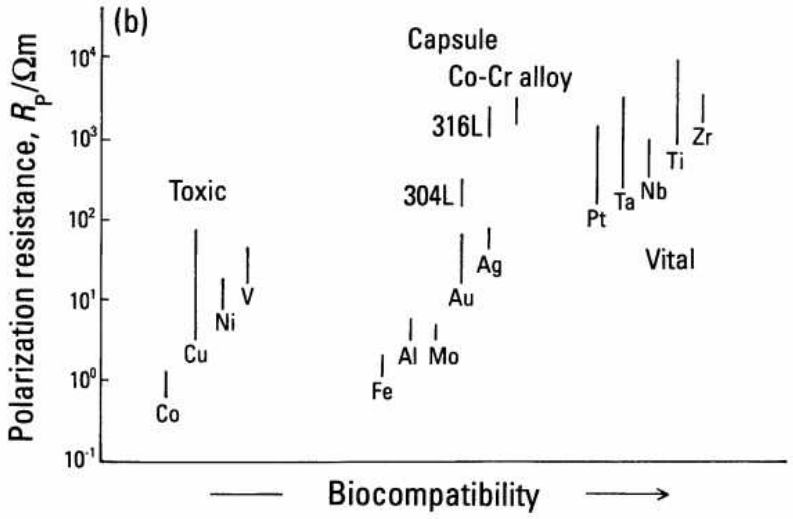


Fig. 2. Polarization resistance and biocompatibility of various metal elements[17].

## Ⅱ. 2. Titanium alloy[18)]

Titanium is a metal with an element number of 22, a silver-white luster and one of the most widely distributed metals on earth. Pure Ti exists as an α phase of a dense hexagonal packed crystal structure (HCP) at room temperature, but it has an equilibrium transformation point at 882℃ and changes to a β phase of the body-centered cubic lattice (BCC) at temperatures above this temperature. The anodic transformation point is hardly changed by the heating and cooling rate by welding or heat treatment, but varies greatly by the addition of alloying element and appears as a coexistence phase of α + β or a β phase even at room temperature. The main physical properties of pure Ti are as follows. (1). It has a high melting point of 1680℃. (2). The specific gravity is 4.5 g/cm$^2$, which is about 1/2 of the steel. (3). The coefficient of linear expansion is small and about 1/2 of that of austenitic stainless steel. (4). Thermal conductivity is 1/4 of steel, similar to austenitic stainless steels. (5). Young's modulus is small, about 1/2 of austenitic stainless steel.

Ti alloys are classified into α type, near-α type, α + β type, and β type, and their structure is determined by the type, quantity, processing and heat treatment of the alloy added to the pure Ti. Table 1 details the physical properties of unalloyed titanium. Elements such as Al, $O_2$, and $N_2$ that increase the transformation point while expanding the α region are α stabilizing elements, on the other hand, V, Mo, Fe, Cr, Mn and the like which lower the transformation point to enlarge the β region are β stabilizing elements. Zr and Sn are not related to the phase transformation, but are elements reinforcing both α and β phases.

Table 1. Summary of physical properties of pure titanium[18].

| Property | Value |
|---|---|
| Atomic number | 22 |
| Atomic weight (g/mol) | 47.90 |
| Crystal structure | |
| Alpha, hexagonal, closely packed | |
| $c$ (Å) | $4.6832 \pm 0.0004$ |
| $a$ (Å) | $2.9504 \pm 0.0004$ |
| Beta, cubic, body centered | |
| $a$ (Å) | $3.28 \pm 0.003$ |
| Density (g $cm^{-3}$) | 4.54 |
| Coefficient of thermal expansion, $\alpha$, at 20 °C ($K^{-1}$) | $8.4 \times 10^{-6}$ |
| Thermal conductivity (W/(m K)) | 19.2 |
| Melting temperature (°C) | 1668 |
| Boiling temperature (estimated) (°C) | 3260 |
| Transformation temperature (°C) | 882.5 |
| Electrical resistivity | |
| High purity (μΩ cm) | 42 |
| Commercial purity (μΩ cm) | 55 |
| Modulus of elasticity, $\alpha$, (GPa) | 105 |
| Yield strength, $\alpha$, (MPa) | 692 |
| Ultimate strength, $\alpha$, (MPa) | 785 |

### Ⅱ. 2. 1. α titanium alloy[19)]

It is strengthened by adding α phase stabilization element and shows stable property at high temperature. Ti-5Al-2.5Sn is a typical α titanium alloy. In the case of high temperature strength and creep characteristics, α-Ti does not deteriorate in ductility and toughness even at low temperatures and is excellent as a low-temperature structural material. And there are α-stabilizer, such as Al, O, N, and C.

### Ⅱ. 2. 2. near-α titanium alloy[18)]

In order to further improve the creep properties of the α-titanium alloy which exhibits stable high-temperature characteristics, the addition of Al, Zr or the like added 1-2% of the β-phase stabilizing element simultaneously with the strengthening of the α phase solid solution. Systematically, it is α + β titanium alloy close to α phase, and it has high temperature characteristic which is superior to α alloy characteristic of high strength.

### Ⅱ. 2. 3. α+β titanium alloy[18)]

It is an alloy that adds a β phase stabilizing element to an α phase strengthened Ti-Al alloy and enhances solidification in the β phase as well as a heat treatment effect. High strength can be obtained, and heat resistance is excellent. The structure of the α+β alloy is classified into a needle-like α structure and an equiaxed α structure according to the shape of the α phase. The needle-like α structure is excellent in creep characteristics and toughness, and the isometric α structure is excellent in tensile properties.

## Ⅱ. 2. 4. β titanium alloy[18-19)]

The quenching phase causes the β phase to remain at room temperature and is in the normal state. The near-stable β phase decomposes into an α phase and a stable β phase by reheating at a relatively low temperature, so this property can be used for heat treatment. β alloy has excellent process ability, high strength can be obtained by heat treatment, and corrosion resistance is excellent. β-stabilizers are Mo, V, Nb, Ta, Fe, W, Cr, Si, Co, Mn, and H. However, the specific gravity is about 10% larger than the α+β alloy and the Young's modulus is about 10% smaller. In addition, since it is a structure of body centered cubic lattice, it has low ductility and toughness at low temperature, and there are problems such as embrittlement caused by ω phase in which metastable β phase is formed at the time of decomposition. Table 2 shows the physical properties of the titanium alloy according to the microstructure.

Table 2. Mechanical properties of some titanium and its alloys[18].

| Alloy designation | Microstructure | Elastic modulus $E$ (GPa) | Yield strength, YS (MPa) | Ultimate strength UTS (MPa) |
|---|---|---|---|---|
| cpTi | α | 105 | 692 | 785 |
| Ti–6Al–4V | α/β | 110 | 850–900 | 960–970 |
| Ti–6Al–7Nb (protasul-100) | α/β | 105 | 921 | 1024 |
| Ti–5Al–2.5Fe | α/β | 110 | 914 | 1033 |
| Ti–12Mo–6Zr–2Fe (TMZF) | Metastable β | 74–85 | 1000–1060 | 1060–1100 |
| Ti–15Mo–5Zr–3Al | Metastable β | 82 | 771 | 812 |
| | Aged β + α | 100 | 1215 | 1310 |
| Ti–0/20Zr–0/20Sn–4/8Nb–2/4Ta+ (Pd, N, O) | α/β | N/A | 726–990 | 750–1200 |
| Ti–Zr | Cast α′/β | N/A | N/A | 900 |
| Ti–13Nb–13Zr | α′/β | 79 | 900 | 1030 |
| Ti–15Mo–3Nb–0.3O (21SRx) | Metastable β + silicides | 82 | 1020 | 1020 |
| Ti–35Nb–5Ta–7Zr (TNZT) | Metastable β | 55 | 530 | 590 |
| Ti–35Nb–5Ta–7Zr–0.4O (TNZTO) | Metastable β | 66 | 976 | 1010 |
| Bone | Viscoelastic composite | 10–40 | – | 90–140 |

## Ⅱ. 3. Titanium alloys as a bio-metallic materials[19].

Metallic materials such as stainless steel, Co-Cr alloys, pure titanium, and titanium alloys have been used for surgical implant materials. The α + β type titanium alloy, such as Ti-6Al-4V ELI, is the most widely used implant material for artificial hip and dental implants because of its high strength and corrosion resistance. However, the toxicity of alloying elements in biomaterial titanium alloys such as Al and V and the high modulus of elasticity compared to bones are steadily being pointed out. Recently, β-type titanium alloys have been developed which have low elastic modulus and superior corrosion resistance and tissue response as compared with α + β-type alloys. Therefore, new β-type titanium alloys composed of non-toxic elements such as Nb, Ta, Zr, Mo, and Sn are used as alloys. Table 3 shows the elastic modulus of each alloy.

Table 3. Young's moduli of conventional biomedical titanium alloys[19].

| Chemical composition (mass%) | Young's modulus (GPa) | |
|---|---|---|
| | S.T. | STA |
| Ti-6Al-4V ELI | 112 | 112 |
| Ti-13Nb-13Zr | 64–77 | 81 |
| Ti-29Nb-13Ta-4.6Zr[b] | 65 | 84 |
| Ti-16Nb-13Ta4-Mo[b] | 91 | 113 |
| Ti-29Nb-13Ta[b] | 76 | 103 |
| Ti-29Nb-13Ta-4Mo[b] | 74 | 73 |
| Ti-29Nb-13Ta-2Sn[b] | 62 | 78 |
| Ti-29Nb-13Ta-4.6Sn[b] | 66 | 69 |
| Ti-29Nb-13Ta-6Sn | 74 | 73 |

[a] ST: as-solutionized; STA: aged after solutionized.
[b] Designed alloys.

## Ⅱ. 4. Surface treatment for titanium alloy

### Ⅱ. 4. 1. Plasma electrolytic oxidation (PEO) process[20-23)]

Table 4 shows various surface modification methods for titanium alloys. Plasma electrolytic oxidation (PEO), which combines high-voltage sparks and electrochemical oxidation, is a novel method to form ceramic coatings on light metals such as Ti and its alloys. In the case of addition of Ca and $PO_4$ ions in the electrolyte induces bonding with bone, it is a convenient technology that is economical and easy to process. These oxide film produced by the electrochemical surface treatment is a thick and uniform porous form. It is also composed of hydroxyapatite and calcium phosphate-based phases, so it has the characteristics of bone inorganic, non-toxic and very high bioactivity and biocompatibility. Such an oxide coating has a controllable shape and composition, excellent bonding strength with a substrate, and excellent corrosion resistance, also, has greater mechanical properties and adhesion than those produced by plasma spraying.

The main reactions occurring at the anode during the plasma oxidation process are as follows:

(1) $Ti \rightarrow Ti^{2+} + 4e^-$

(2) $2H_20 \rightarrow 20^{2-} + 4H^+$

(3) $2H_20 \rightarrow 0_2(gas) + 4H^+ + 4e^-$

(4) $Ti^{2+} + 20^{2-} \rightarrow TiO_2 + 2e^-$

The electrode reaction during electrolysis in aqueous solution is shown in Fig. 3. When a voltage is applied to an aqueous solution containing an

electrolyte, oxygen gas is generated on the surface of the anode or an oxidation reaction of the metal occurs. In the cathode, hydrogen gas is generated or a reduction reaction occurs.

Table 4. Overview of surface modification methods for titanium and its alloys for implants[18].

| Surface modification methods | Modified layer | Objective |
|---|---|---|
| Mechanical methods | | |
| Machining<br>Grinding<br>Polishing<br>Blasting | Rough or smooth surface formed by subtraction process | Produce specific surface topographies; clean and roughen surface; improve adhesion in bonding |
| Chemical methods | | |
| Chemical treatment | | |
| Acidic treatment | <10 nm of surface oxide layer | Remove oxide scales and contamination |
| Alkaline treatment | ~1 μm of sodium titanate gel | Improve biocompatibility, bioactivity or bone conductivity |
| Hydrogen peroxide treatment | ~5 nm of dense inner oxide and porous outer layer | Improving biocompatibility, bioactivity or bone conductivity |
| Sol–gel | ~10 μm of thin film, such as calcium phosphate, $TiO_2$ and silica | Improve biocompatibility, bioactivity or bone conductivity |
| Anodic oxidation | ~10 nm to 40 μm of $TiO_2$ layer, adsorption and incorporation of electrolyte anions | Produce specific surface topographies; improved corrosion resistance; improve biocompatibility, bioactivity or bone conductivity |
| CVD | ~1 μm of TiN, TiC, TiCN, diamond and diamond-like carbon thin film | Improve wear resistance, corrosion resistance and blood compatibility |
| Biochemical methods | Modification through silanized titania, photochemistry, self-assembled monolayers, protein-resistance, etc. | Induce specific cell and tissue response by means of surface-immobilized peptides, proteins, or growth factors |
| Physical methods | | |
| Thermal spray | | |
| Flame spray<br>Plasma spray<br>HVOF<br>DGUN | ~30 to ~200 μm of coatings, such as titanium, HA, calcium silicate, $Al_2O_3$, $ZrO_2$, $TiO_2$ | Improve wear resistance, corrosion resistance and biological properties |
| PVD | | |
| Evaporation<br>Ion plating<br>Sputtering | ~1 μm of TiN, TiC, TiCN, diamond and diamond-like carbon thin film | Improve wear resistance, corrosion resistance and blood compatibility |
| Ion implantation and deposition | | |
| Beam-line ion implantation<br>PIII | ~10 nm of surface modified layer and/or ~μm of thin film | Modify surface composition; improve wear, corrosion resistance, and biocompatibility |
| Glow discharge plasma treatment | ~1 nm to ~100 nm of surface modified layer | Clean, sterilize, oxide, nitride surface; remove native oxide layer |

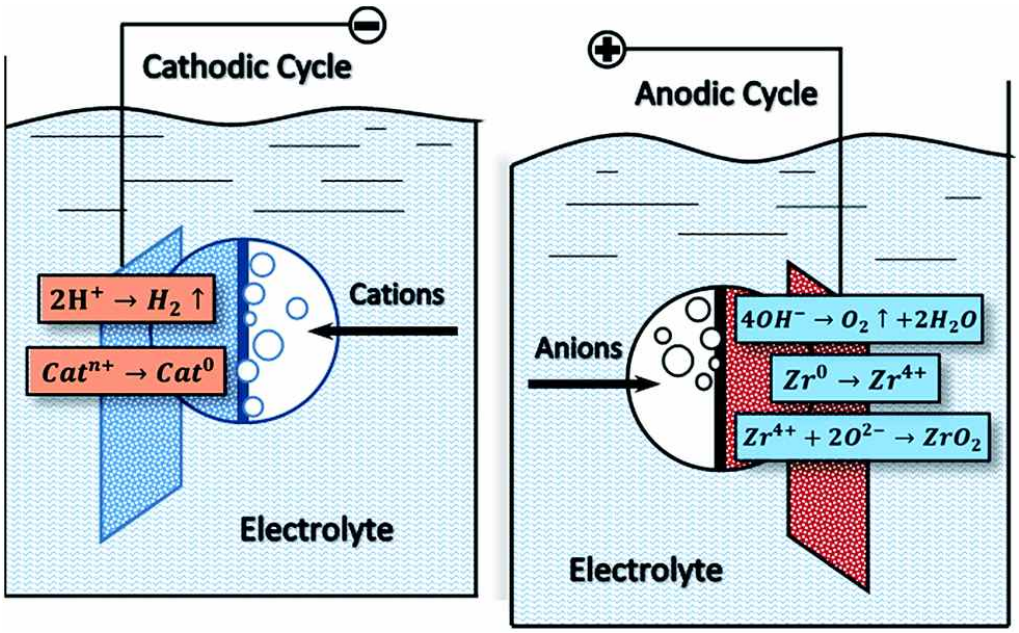


Fig. 3. Schematic diagrams of electrode processes in electrolysis of aqueous solutions[18].

## Ⅱ. 4. 2. Magnesium (Mg) in the bone[14)]

It has been reported that trace elements essential in the human body play an important role in bone formation because they affect bone density. Information on biological phosphates is shown in Table 5, and the chemical composition present in the human body is shown in Table 6. Among the various elements, magnesium (Mg) is one of the major substituents of calcium (Ca), and the amounts contained in enamel, dentine, and bone are 0.2 wt.%, 1.1 wt.%, and 0.6 wt.%, respectively. And Mg is the fourth most abundant ion present in the human body. Mg has a structure that can be easily substituted in the HA lattice and is known as a Ca substitute, and can be represented by the formula $Ca_{10-x}$ $Mg_x$ $(PO_4)_6$ $(OH)_2$.

Mg ions are known to inhibit crystallization and stimulate the nucleation of large amounts of apatite nuclei and play an important role in the proliferation of bone metabolism by affecting osteoblast and osteoclast activity. In the bone, Mg stimulates the immature (irregular) bone to transform it into a more crystalline and mature bone. Substitution of magnesium in Ca-deficient HA lattice is expected to have superior biocompatibility of Mg-HA and comparable to hard tissue. It is expected that the control of the amount of $Mg^{2+}$ substitution in the Mg-HA solution will control the bioactivity as a result of solubility, crystallinity, and particle shape. Therefore, surface modification helps improve the activity between the implant and bone.

## Ⅱ. 4. 3. Zinc (Zn) in the bone[16)]

Zn is known as a trace element essential for life. It also acts as a cofactor for a number of enzymes, including enzymes involved in DNA and RNA replication and protein synthesis. It is one of the major substitutional ions of calcium and is contained in enamel, dentin, and bone at 263 ppm, 173 ppm, and 39 ppm, respectively, Zn is the eighth most abundant cation in the extracellular matrix of the bone. Table 5 shows comparative compositions of enamel, dentin, and bone. Zn inhibits osteoclast differentiation and stimulates osteoclast activity to promote bone formation. Zn deficiency reduces bone mineral density by decreasing nucleic acid metabolism, protein production and bone growth and *in vivo* activity. When Zn is added to the HA lattice lacking Ca, it is expected that β-TCP will be easily formed, so that it has excellent biocompatibility and exhibits properties equivalent to hard tissue

The following is a chemical reaction to replace Ca and Zn ions.

(5) $Ca^{2+} + HPO_4^{2-} \rightarrow CaHPO_4$

(6) $3CaHPO_4 \rightarrow Ca_3(PO_4)_2 + H_3PO_4$

(7) $3Zn^{2+} + 2H_2PO_4^{-} + 2H^{+} + 4H_2O + 6e \rightarrow Zn_3(PO_4)_2 \cdot 4H_2O + 3H_2 \uparrow$

$Zn_3(PO_4)_2 \cdot 4H_2O$ is a major component of the Zn-Ca-P coating.

Table 5. Properties, preparations, and occurrence of the biologically relevant phosphates[11].

| Abbreviation | Formula | Name (mineral) | Ca/P ratio | $pK_{sp}$ (25 °C)[a] | pH stability[a] | Main preparation methods | Occurrence in biological tissues |
|---|---|---|---|---|---|---|---|
| HA | $Ca_{10}(PO_4)_6(OH)_2$ | Hydroxyapatite | 1.67 | 116.8 | 9.5–12 | (i) Titration of $Ca(OH)_2$ with $H_3PO_4$<br>(ii) Dropwise addition of $HPO_4^{2-}$ solution to $Ca^{2+}$ solution, pH > 9<br>(iii) Hydrolysis from other phosphates | Bone, dentin, enamel, dental calcifications, urinary stones, atherosclerotic plaques |
| OCP | $Ca_8H_2(PO_4)_6{\cdot}5H_2O$ | Octacalcium phosphate | 1.33 | 96.6 | 5.5–7.0 | Dropwise addition of $Ca(Ac)_2$ to $HPO_4^{2-}$/$H_2PO_4^-$ solutions at 60 °C, pH 5 | Dental and urinary calculi |
| β-TCP | $Ca_3(PO_4)_2$ | β-Tricalcium phosphate (whitlokite) | 1.5 | 28.9 | [b] | (i) Solid-state reaction of $CaCO_3$ and DCPD at 900 °C<br>(ii) Thermal conversion of CDHA | Dental and urinary calculi, soft-tissue deposits, artritic cartilage, usually present as β-TCMP |
| α-TCP | $Ca_3(PO_4)_2$ | α-Tricalcium phosphate | 1.5 | 25.5 | [b] | Heat treatment of β-TCP at 1300 °C | Not found |
| ACP | $Ca_x(PO_4)_y{\cdot}nH_2O$ | Amorphous calcium phosphate | 1.2–2.2 | [c] | [b] | Fast mixing of $Ca^{2+}$ and $HPO_4^{2-}$ solutions, RT | Soft-tissue calcifications |
| MCPM | $Ca(H_2PO_4)_2{\cdot}H_2O$ | Monocalcium phosphate monohydrate | 0.5 | 1.14 | 0–2 | Titration of $H_3PO_4$ with $Ca(OH)_2$ in strong acidic environment | Not found |
| MCPA | $Ca(H_2PO_4)_2$ | Anhydrous monocalcium phosphate | 0.5 | 1.14 | [b] | Heat treatment of MCPM at $T > 100$ °C | Not found |
| DCPD | $CaHPO_4{\cdot}2H_2O$ | Dicalcium phosphate dihydrate (brushite) | 1.0 | 6.59 | 2–6 | Dropwise addition of a $Ca^{2+}$ solution to a $HPO_4^{2-}$ solution at 60 °C, pH 4 | Dental calculi, urinary stones chondrocalcinosis |
| DCPA | $CaHPO_4$ | Anhydrous dicalcium phosphate (monetite) | 1.0 | 6.90 | [b] | Heat treatment of DCPD at $T > 100$ °C | Not found |
| TTCP | $Ca_4(PO_4)_2$ | Tetracalcium phosphate | 2.0 | 38–44 | [b] | Solid-state reaction of DCPA with $CaCO_3$ at high $T$ | Not found |
| CDHA | $Ca_{10-x}(HPO_4)_x(PO_4)_{6-x}(OH)_{2-x}$ | Calcium-deficient hydroxyapatite | 1.5 | 85.1 | 6.5–9.5 | Hydrolysis of ACP or α-TCP | Not found |

Table 6. Comparative composition of human enamel, dentin, and bone[11].

| | Enamel | Dentin | Bone |
|---|---|---|---|
| Ca (wt.%) | 37.6 | 40.3 | 36.6 |
| P (wt.%) | 18.3 | 18.6 | 17.1 |
| $CO_2$ (wt.%) | 3.0 | 4.8 | 4.8 |
| Na (wt.%) | 0.70 | 0.1 | 1.0 |
| K (wt.%) | 0.05 | 0.07 | 0.07 |
| Mg (wt.%) | 0.2 | 1.1 | 0.6 |
| Sr (wt.%) | 0.03 | 0.04 | 0.05 |
| Cl (wt.%) | 0.4 | 0.27 | 0.1 |
| F (wt.%) | 0.01 | 0.07 | 0.1 |
| Zn (ppm) | 263 | 173 | 39 |
| Ba (ppm) | 125 | 129 | |
| Fe (ppm) | 118 | 93 | |
| Al (ppm) | 86 | 69 | |
| Ag (ppm) | 0.6 | 2 | |
| Cr (ppm) | 1 | 2 | 0.33 |
| Co (ppm) | 0.1 | 1 | <0.025 |
| Sb (ppm) | 1 | 0.7 | |
| Mn (ppm) | 0.6 | 0.6 | 0.17 |
| Au (ppm) | 0.1 | 0.07 | |
| Br (ppm) | 34 | 114 | |
| Si (ppm) | | | 500 |
| Ca/P | 1.59 | 1.67 | 1.65 |

# Ⅲ. MATERIALS AND METHODS

## Ⅲ. 1. Preparation of Ti-40Ta-xZr alloys

Ti-40Ta-xZr alloys (x = 0 and 15 wt.%) were prepared using a vacuum arc-melting furnace. All ingots were melted 6 times, and the cast alloys were heat treated at 1100 ℃ for 1 h in an Ar atmosphere and water-quenched at 0 ° C to ensure homogenization. Samples for study were cut to 50 mm thickness using a high-speed diamond cutting machine (Accutom-5, Struers, Denmark) with 2000 rpm speed. Polishing was carried out using SiC paper of different grades ranging from 100 to 2000, ending with an alumina slurry (3 μm particle size). Finally, the polished samples were ultrasonically cleaned in ethanol, rinsing distilled water, and then dried in air. The compositions of alloys were detected by X-Ray Fluorescence (XRF, Analyzer Mde-Alloy, Analyzer Serial number-581331, OLYMPUS, Japan)

## Ⅲ. 2. Microstructure observation of alloys

The etching treatment was performed in Keller's reagent with 2 ㎖ HF, 3 ㎖ HCl, 5 ㎖ $HNO_3$, and 190 ㎖ $H_2O$. Microstructure observations of Ti-40Ta-xZr alloy was analyzed by optical microscopy (OM, olympus, BX 60M, Japan), and field-emission scanning electron microscopy (FE-SEM, S-4800 Hitachi, Japan).

## Ⅲ. 3. Plasma electrolytic oxidation(PEO)

The washed specimen is used as the anode and the carbon rod is used as the cathode. Pulsed DC power of 280 V was applied to all specimens for 3 minutes. The electrolyte used in PEO was prepared by mixing calcium acetate monohydrate ($Ca(CH_3COO)_2 \cdot H_2O$), calcium glycerophosphate ($C_3H_7CaO_6P$), zinc acetate dehydrate ($(CH_3CO_2)_2Zn \cdot 2H_2O$), and magnesium acetate tetrahydrate ($(CH_3COO)_2Mg \cdot 4H2O$). The concentration of the electrolytic solution is shown in Table 7. When a coating film was formed on the alloy, it was washed with distilled water and ethanol, and then dried in air.

Table 7. The condition of plasma electrolytic oxidation

| Experimental Condition / Solutions | Composition of Electrolyte | | | |
|---|---|---|---|---|
| | Calcium Acetate ($Ca(CH_3COO)_2 \cdot 2H_2O$) | Calcium Glycerophosphate ($C_3H_7CaO_6P$) | Magnesium acetate tetrahydrate ($(CH_3COO)_2Mg \cdot 4H_2O$) | Zinc acetate dehydrate ($(CH_3CO_2)_2Zn \cdot 2H_2O$) |
| CaP | 0.15 M | 0.02 M | 0 | 0 |
| CaP+Mg,Zn ions | 0.135 M | 0.02 M | 0.0075M | 0.0075M |

## Ⅲ. 4. Analysis of surface characteristics for Ti-40Ta-xZr alloys

The surface characterization of the PEO-coated surface is analyzed by field emission scanning electron microscopy (FE-SEM, S-4800 Hitachi, Japan) and energy dispersive X-ray spectroscopy (EDS, Inca Program, Oxford, UK). The surfaces of Ti-40Ta-xZr alloys were observed by optical microscopy (OM, olympus, BX 60M, Japan). The surface area of the pores was measured using an image analyzer (Image J, Wayne Rasband, USA). Also, the phase of the specimen was analyzed with a thin film X-ray diffractometer (TF-XRD, X'pert Philips, Netherlands) at a radiation scanning range of 10° to 85°. Phase was identified by matching each characteristics peak with JCPDS card.

## Ⅲ. 5. Mechanical properties test

### Ⅲ. 5. 1. Vickers hardness

The mechanical property of the Ti-40Ta-xZr alloys were analyzed by surface hardness. It was measured through vickers hardness tester(DM-20, AFFRI, Italy) with a load of 300 gf applied for 5s on the ten regions of each alloy.

### Ⅲ. 5. 2. Surface roughness

Surface roughness measurements were obtained by using Atomic force microscopy (Park XE-100 AFM, Park Systems, Korea) with Scan size 10.00㎛, Scan rate 0.10Hz, Z servo grain 0.90, Set point 6.91nm, Drive 20.0%. amplitude 20.23nm.

### Ⅲ. 5. 3. Measurement of elastic modulus by nano-indentation analysis

The elastic modulus of the Ti-40Ta-xZr alloys was measured using a nano-indentation tester with allowable load range of 500 mN, a pulling speed of 10 N / min, depth range fine range 40 ㎛, large range 200 ㎛ (TTX-NHT3, Anton paar, Austrial).

## Ⅲ. 6. Surface wettability measurement

Surface wettability test was performed on the surface and anodized surface using a water contact angle goniometer (Kruss DSA100, Germany) in distilled water drop mode with 6 $\mu\ell$ drops. Water solution was used as the probe liquids in our research. The contact angles were measured by sessile droplet method with a help of contact angle meter which contains an automatic drop deposition system and a video camera.

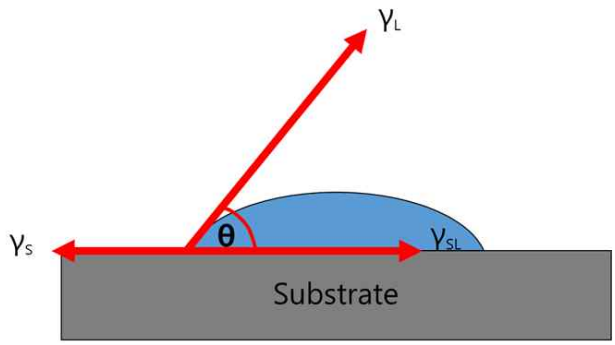


$\gamma_S$ : Surface free energy of solid
$\gamma_L$ : Surface tension of liquid
$\gamma_{SL}$ : Interfacial tension between liquid and solid

$$\gamma_S = \gamma_L \cdot \cos\theta + \gamma_{SL}$$

Fig. 4. Equilibrium wetting state of liquid.

## Ⅲ. 7. Cell culture

HEK cell 293 (Human embryonic kidney cell 293) were cultured on the specimens for cell proliferation test. Cells were plated in α minimum essential medium (MEM, WELGENE, Korea). Cells were cultured in an atmosphere of 37 ℃ at 95% $O_2$, and 5% $CO_2$. Sub-culture medium was changed every third days. The cell monolayer was washed with phosphate buffered saline (PBS), and cultured in trypsin-DTA solution(0.05% trypsin, 0.53 mM EDTA·4Na, phenol red in HBSS) at 37 ℃ for 10 minutes to separate the cells. Cells were seeded on a Ti alloy at a concentration of 9.2 × $10^6$ cells / well on a 24-well plate and grown on the coated surface for 24 h. The samples were washed with PBS and fixed with 10% formaldehyde at 4 ℃ for 12 hours. After fixing, the specimens were dehydrated with ethanol. The morphology of the attached cells was observed using field-emission scanning electron microscopy (FE-SEM).

# IV. RESULTS AND DISCUSSION

## IV. 1. Microstructure observation and phase analysis of Ti-40Ta-xZr alloys

Fig. 5 shows the X-ray fluorescence (XRF) results of the Ti-40Ta-xZr alloys for confirmation of chemical composition. As a result of chemical composition of the homogenized alloy, it was confirmed that the chemical composition of each alloy was very similar to that of the designed alloy. Therefore, alloys were well manufactured from these results.

Fig. 6 and Fig. 7 show the OM and FE-SEM images of Ti-40Ta-xZr alloys after heat treatment at 1050 ℃ for 1h in Ar atmosphere, followed by 0 ℃ water quenching. Ti-40Ta-0Zr, Ti-40Ta-3Zr, and Ti-40Ta-7Zr (Fig. 7, Fig.8- a,b,and c) show the lath and needle like structures of martensite, whereas in Ti-40Ta-15Zr (Fig. 6, Fig.7- d), needle-like structures were hardly formed and it is mainly composed of equiaxed structure. Previous studies have shown that the structure of the tissue has been altered by the content of tantalum added to the titanium alloy. The hexagonal(α') martensite structure was observed at 26% Ta content, the orthorhombic (α") martensite at 26 ~ 52% and the single-phase metastable bcc (body-centered cubic) (β) at Ta content over 65% [24-25]. Despite of the fact that the content of Ta did not increase to 65%, the observation of the equiaxed structure in Fig. 6, Fig. 7 (d) is attributed to the influence of Zr. Zr was not considered as a β stabilizing element in the Ti alloy, but caused a displacement of the martensitic transformation temperature due to the β stabilizing element[3]. Therefore, it is considered that Zr is influenced by the β-type Ti alloy because Ta, which is a β stabilizing element, is changed by addition of Zr which is a neutral element. Also, the phase transformation of Ti-40Ta-xZr alloys was found to be sensitive to Zr content because the microstructure was greatly affected by the weight of Zr[26].

Fig. 8 shows the X-ray diffraction (XRD) peaks of results of Ti-40Ta-xZr alloys microstructure homogenized for 1 hour at 1050 ℃ in Ar atmosphere, followed by 0 ° C water quenching. In Fig. 8, peaks of the α" and β phases were detected but, did not show metastable ω phase. In the case of Ti-40Ta-xZr alloys (x = 0, 3, 7 wt.%), the peaks of the hexagonal martensitic structure mainly appear at 2Θ = 34°, 36°, 39°, 52°, and 74 to 77°, these peaks occur from the needle-like structure as shown in Fig. 6 and Fig. 7. On the contrary, in the case of Ti-40Ta-15Zr alloy, peaks of the equiaxed β phase are shown at 2Θ = 38°, 54° and 69°, which can be seen in the equiaxed structure of Fig. 6 and Fig. 7. As the amount of Zr increased, the β phase peak increased. It is confirmed that phase transformation from the α"-hexagonal structure to the β-body-centered cubic is a substitution effect of Zr on the transformation temperature, and proceeds as the content of Zr increases[27].

As a result, it can be seen that the microstructure of the Ti-40Ta-xZr alloy and the XRD pattern have a significant influence on the content of Zr.

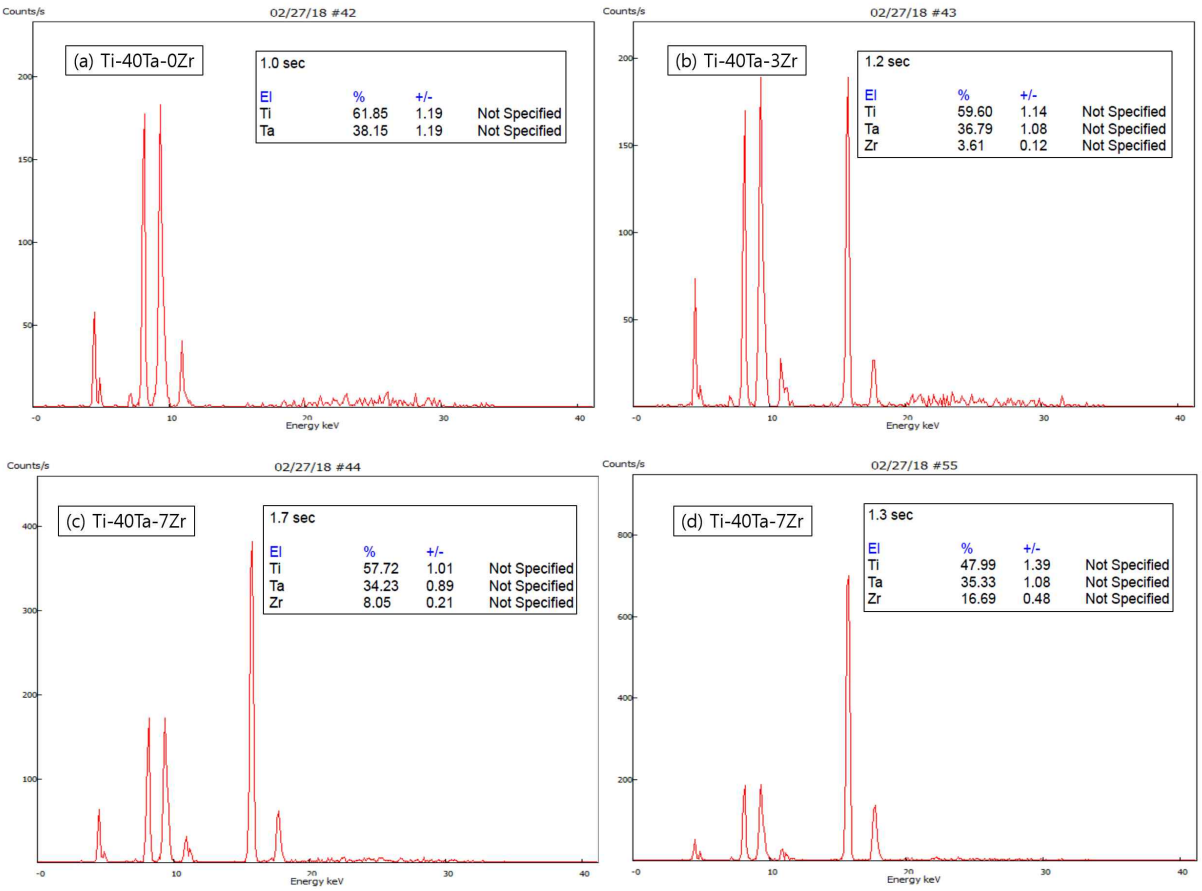


Fig. 5. XRF results of Ti-40Ta-xZr alloys after heat treatment at 1050 ℃ for 1h in Ar atmosphere, followed by 0 ℃ water quenching: (a) Ti-40Ta-0Zr, (b) Ti-40Ta-3Zr, (c) Ti-40Ta-7Zr, and (d) Ti-40Ta-15Zr.

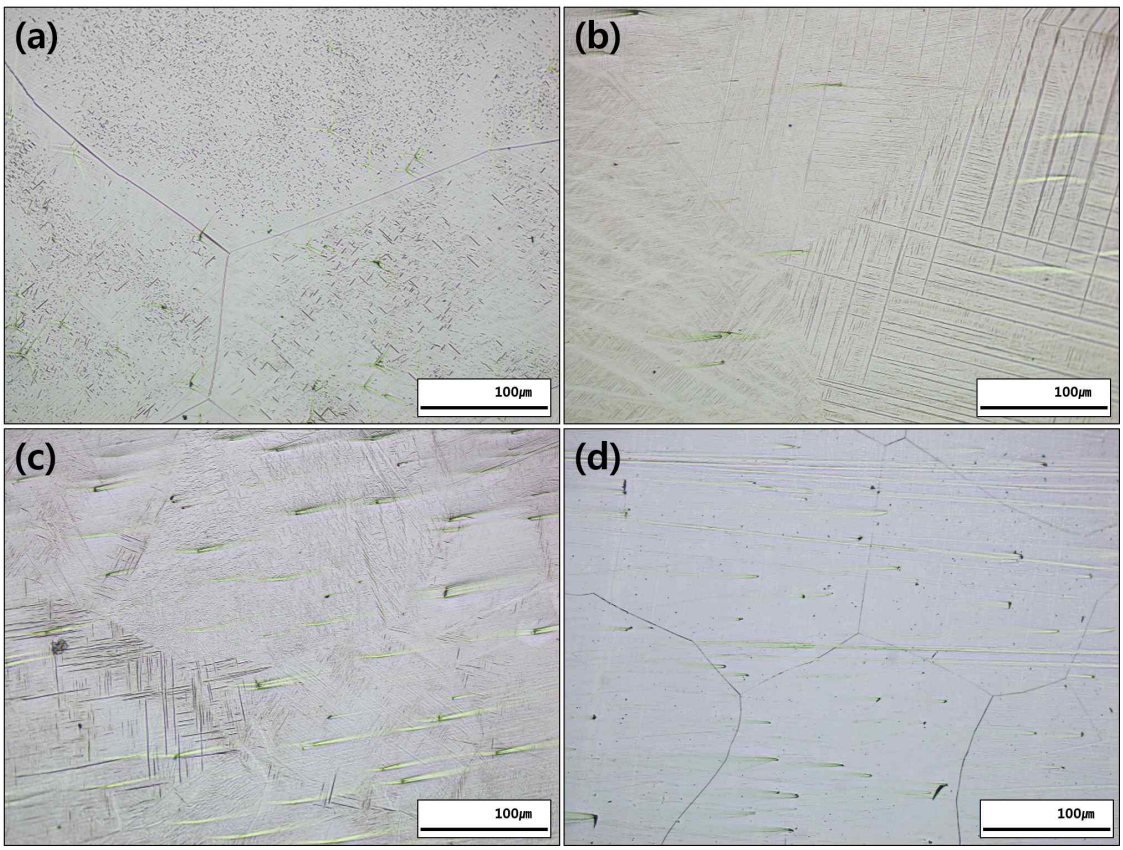


Fig. 6. Optical microstructures of Ti-40Ta-xZr alloys after heat treatment at 1050 ℃ for 1h in Ar atmosphere, followed by 0 ℃ water quenching: (a) Ti-40Ta-0Zr, (b) Ti-40Ta-3Zr, (c) Ti-40Ta-7Zr, and (d) Ti-40Ta-15Zr.

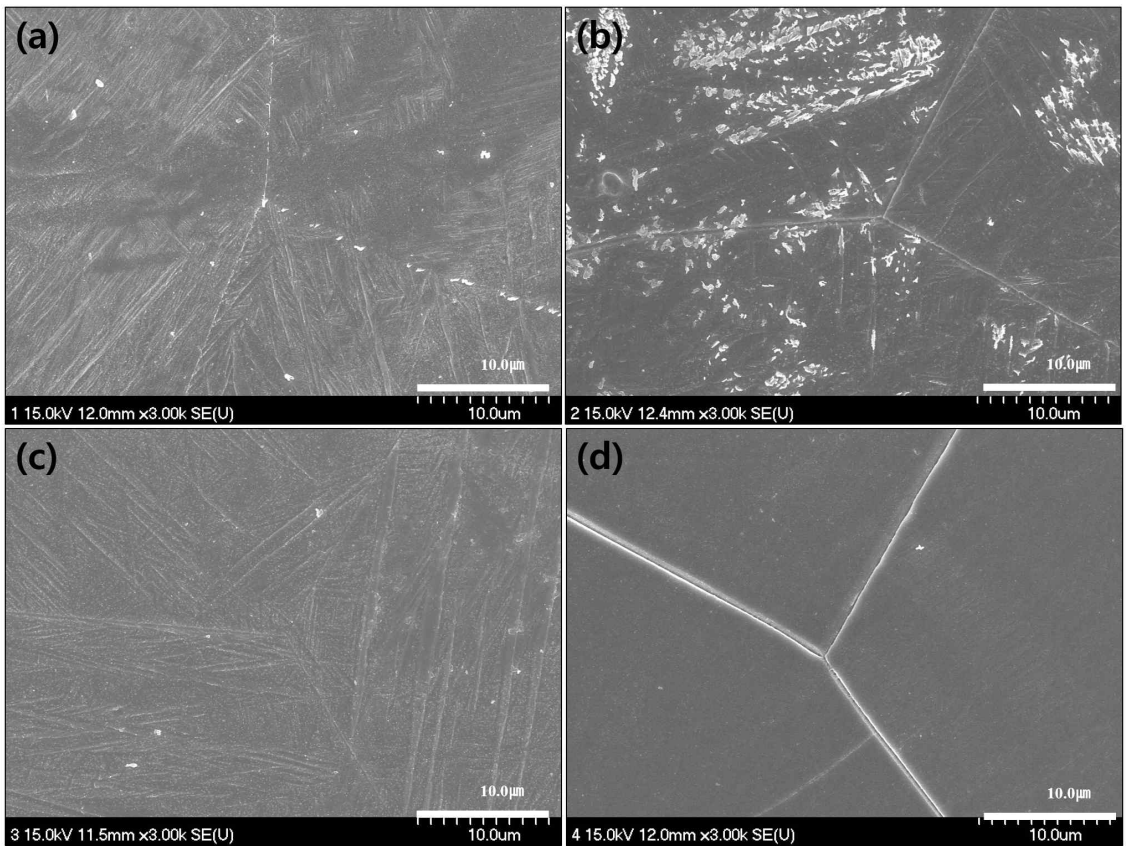


Fig. 7. FE-SEM images of Ti-40Ta-xZr alloys after heat treatment at 1050 ℃ for 1h in Ar atmosphere, followed by 0 ℃ water quenching: (a) Ti-40Ta-0Zr, (b) Ti-40Ta-3Zr, (c) Ti-40Ta-7Zr, and (d) Ti-40Ta-15Zr.

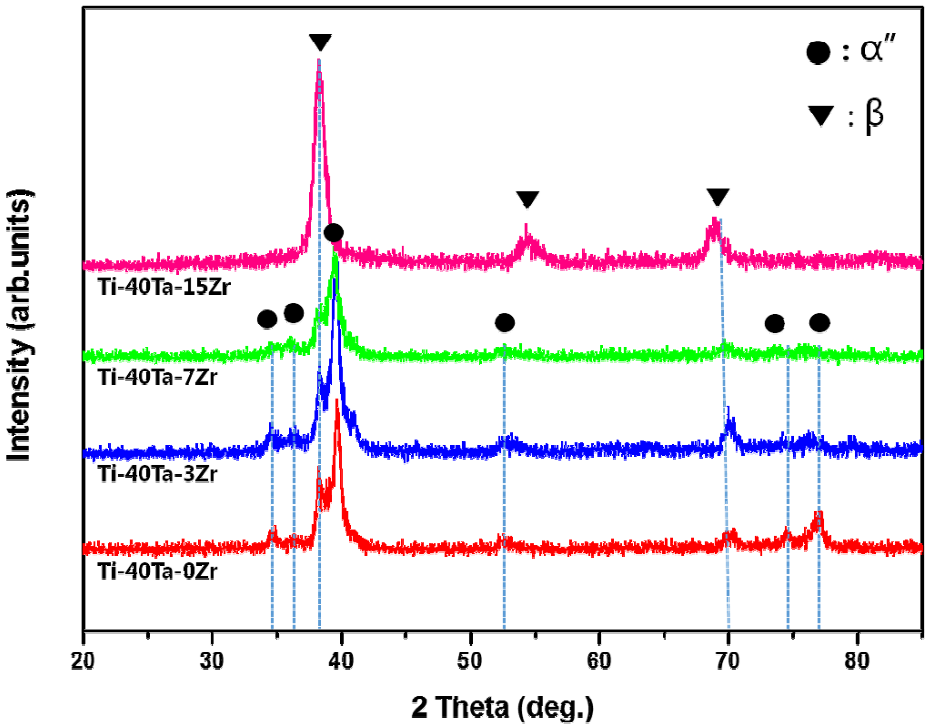


Fig. 8. XRD results of Ti-40Ta-xZr alloys after heat treatment at 1050 ℃ for 1 h in Ar atmosphere, followed by 0℃ water quenching.

## Ⅳ. 2. Mechanical properties of Ti-40Ta-xZr alloys

### Ⅳ. 2. 1. Surface hardness of Ti-40Ta-xZr alloys

Fig. 9 shows the Vickers hardness results. The Vickers hardness value of water quenched Ti-40Ta-xZr alloys shown in Table 8. The highest Vickers hardness value was 314Hv for the Ti-40Ta-0Zr alloy and the lowest Vickers hardness value was 292Hv for the Ti-40Ta-15Zr alloy. The content of Zr increases, phase transformation from α"-hexagonal structure to the β-body-centered cubic was occurred and the alloy becomes sensitive to the indentation, resulting in a lower hardness value[28]. In the case of addition of Zr content to Ti-40Ta alloy, the matrix of Ti-40Ta-xZr alloys was changed to a β phase, therefore, the value of hardness was lowered. And surface roughness of Ti-40Ta-xZr alloys decreased as Zr content increased due formation of needle-like martensitic structure.

### Ⅳ. 2. 2. Nano-indentation results of Ti-40Ta-xZr alloys

Fig. 10 showed the graphs of the nano-indentation test for elastic modulus measurements. The elastic modulus was measured using nano-indentation. The lowest elastic modulus was 88 GPa at the Ti-40Ta-15Zr alloys with the highest content of Zr. The elastic modulus measurements are shown in Table 8. As the content of Zr increased, the elastic modulus tended to decrease gradually. The value of elastic modulus is reported to decrease as the β phase increases. A high modulus of elasticity results in a stress shielding effect, which can lead to osteoporosis or destruction, and therefore alloys with a low modulus of elasticity similar to bone have been developed[18-19]. In this study, lower elastic modulus can be obtained by addition of Zr to Ti-40Ta alloy.

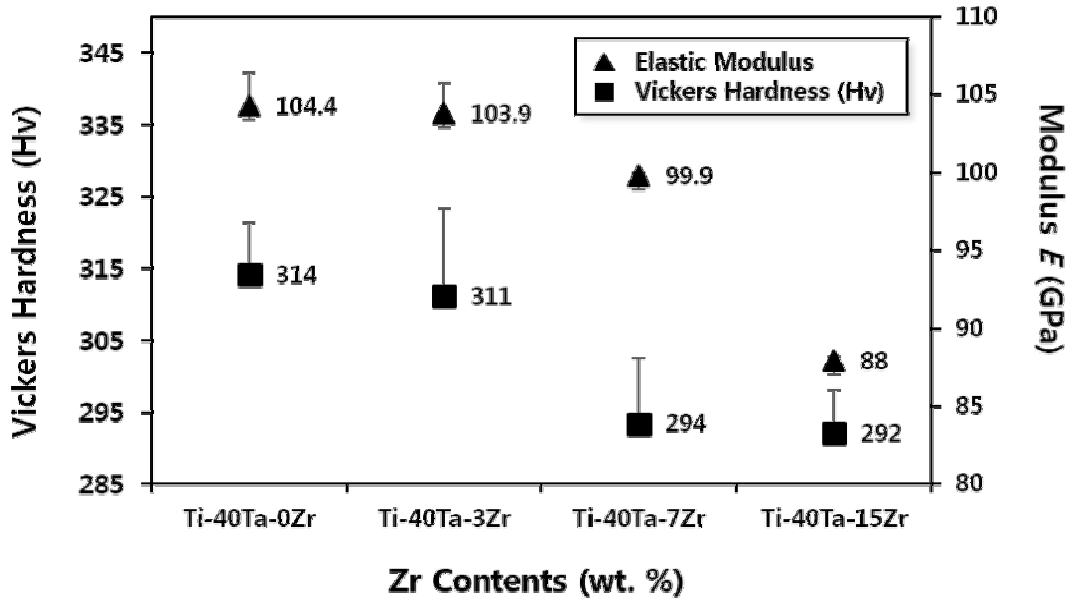


Fig. 9. Vickers hardness values of Ti-40Ta-xZr alloys after heat treatment at 1050 ℃ for 1h in Ar atmosphere followed by 0℃ water quenching.

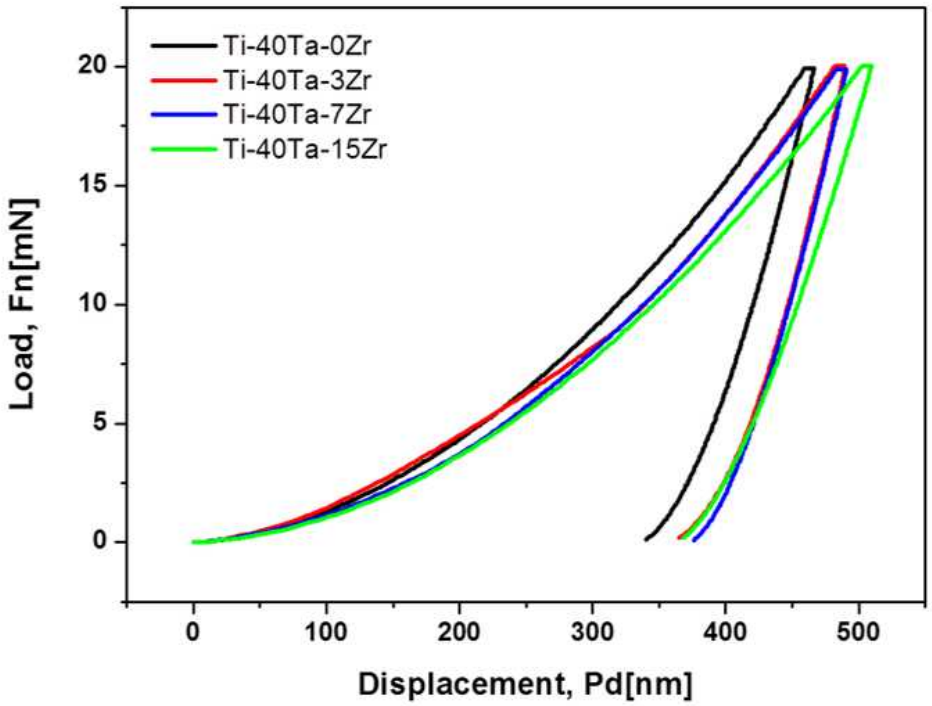


Fig. 10. Nano-indentation test results of Ti-40Ta-xZr alloys after heat treatment at 1050 ℃ for 1h in Ar atmosphere followed by 0℃ water quenching.

Table 8. Young's modulus and Vickers hardness value of Ti-40Ta-xZr alloys.

| Samples / Properties | Young's Modulus (E) [GPa] | Vickers Hardness [Hv] |
|---|---|---|
| Ti-40Ta-0Zr | 104.4 | 314 ± 7.4863 |
| Ti-40Ta-3Zr | 103.9 | 311 ± 12.5716 |
| Ti-40Ta-7Zr | 99.9 | 294 ± 9.4187 |
| Ti-40Ta-15Zr | 88.0 | 292 ± 6.0928 |

## IV. 3. Surface properties of PEO coated Ti-40Ta-xZr alloys

Fig. 11 and 12 show the surface morphology of the PEO coating in the various electrolytes. Fig. 11 is in Ca, P electrolyte, and Fig. 12 is in electrolyte of Ca, P, Mg, and Zn ions. Also, Fig. 11 and 12 (a, a-1)~(d, d-1) are Ti-40Ta-0Zr, Ti-40Ta-3Zr, Ti-40Ta-7Zr, and Ti-40Ta-15Zr, respectively. During the anodic oxidation process, $TiO_2$ molecules are formed to form a soft oxide layer, and a high electric field between the inner and outer boundary surfaces of the film induces local destruction of the $TiO_2$ layer, resulting in pore formation along with characteristic surface morphology. The pores of the PEO-treated surface are a typical plasma-coated structure called the micro-discharge channel. The high temperature and high pressure within the micro discharge channels create porous coarse coating surfaces. It is also a typical plasma coating structure in which pores called micro-discharge channels are formed at the surface during the PEO treatment process. Simulations of plasma chemical processes have shown that the formation of composite oxides as well as oxides of the coating alloys is possible in the coating discharge channels[29-32]. The chemical bonding occurs in such fine discharge channels to form oxides such as $TiO_2$, $Ta_2O_5$, and $ZrO_2$.

Table 9 shows the calculation of the area occupied by the pores at the surface through the image J program analysis. In the FE-SEM image, the Ti-40Ta-xZr alloys tends to increase in pore size as the Zr content increases and pores are also observed within the pore. Even though generally limiting the size of the pores can be formed by increasing the voltage or time of the plasma coating[29], the pore size can be controlled by adjusting the content of Zr. Also, when the content of Zr increases, the distance of the pores increases from 1.22㎛ to 3.06 ㎛. The increase in pore size and distance seems to reduce the roughness.

Fig. 13 shows the XRD pattern on the PEO-surface treatment. Various oxides were detected on the PEO-treated surface of the alloy. As the content of Zr increases in the Ti-Ta alloy, the anatase phase of $TiO_2$ decreased and $ZrO_2$ and $Ta_2O_5$ gradually increased.

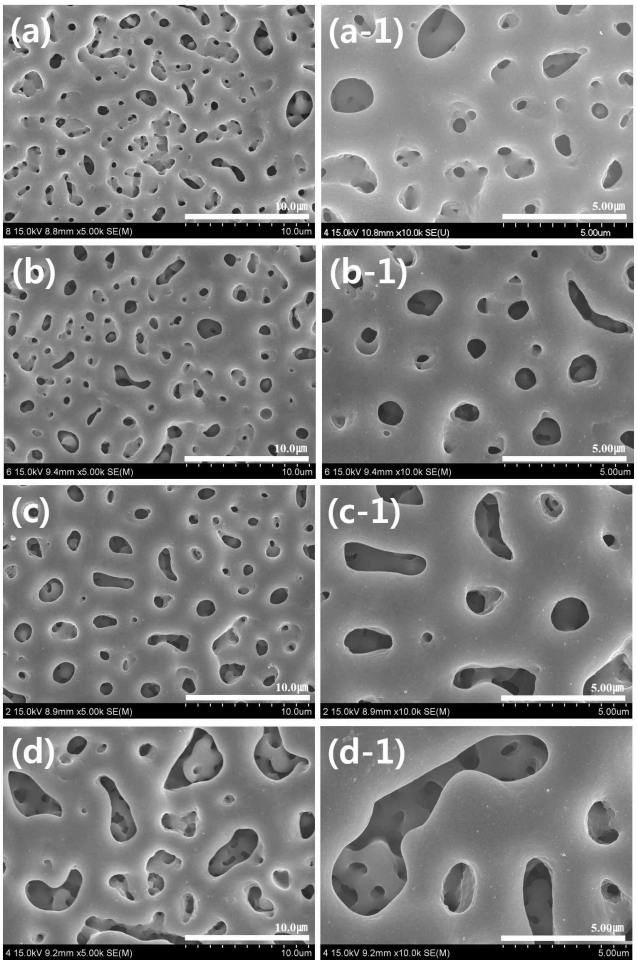


Fig. 11. FE-SEM images of PEO-treated Ti-40Ta-xZr alloys in 0.15 M calcium acetate monohydrate + 0.02 M calcium glycerophosphate: (a, a-1) Ti-40Ta-0Zr, (b, b-1) Ti-40Ta-3Zr, (c, c-1) Ti-40Ta-7Zr, and (d, d-1) Ti-40Ta-15Zr.

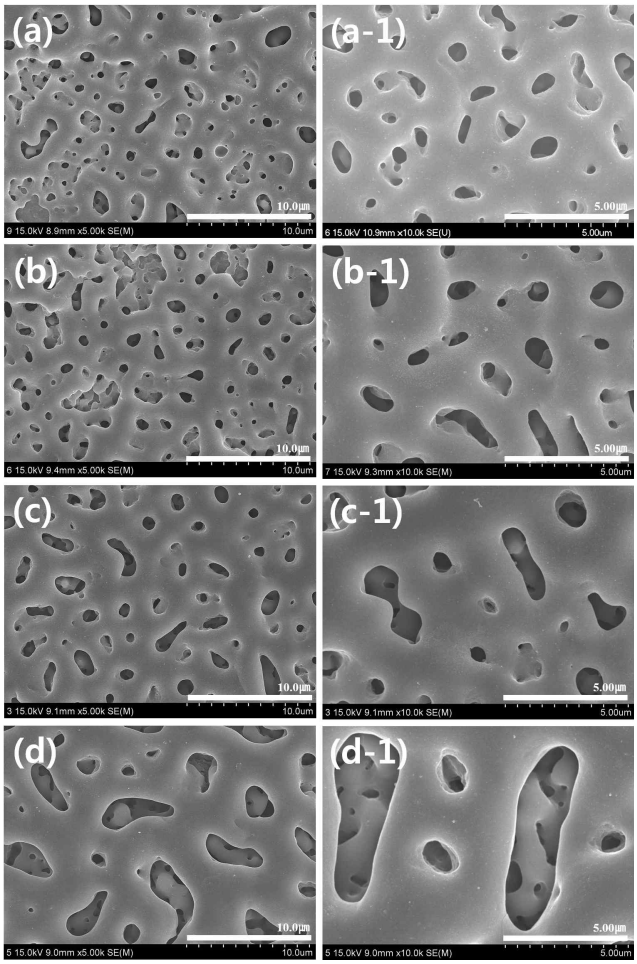


Fig. 12. FE-SEM images of PEO-treated Ti-40Ta-xZr alloys in 0.135 M calcium acetate monohydrate + 0.02 M calcium glycerophosphate + 0.0075 M magnesium acetate tetrahydrate + 0.0075 M zinc acetate dehydrate: (a, a-1) Ti-40Ta-0Zr, (b, b-1) Ti-40Ta-3Zr, (c, c-1) Ti-40Ta-7Zr, and (d, d-1) Ti-40Ta-15Zr.

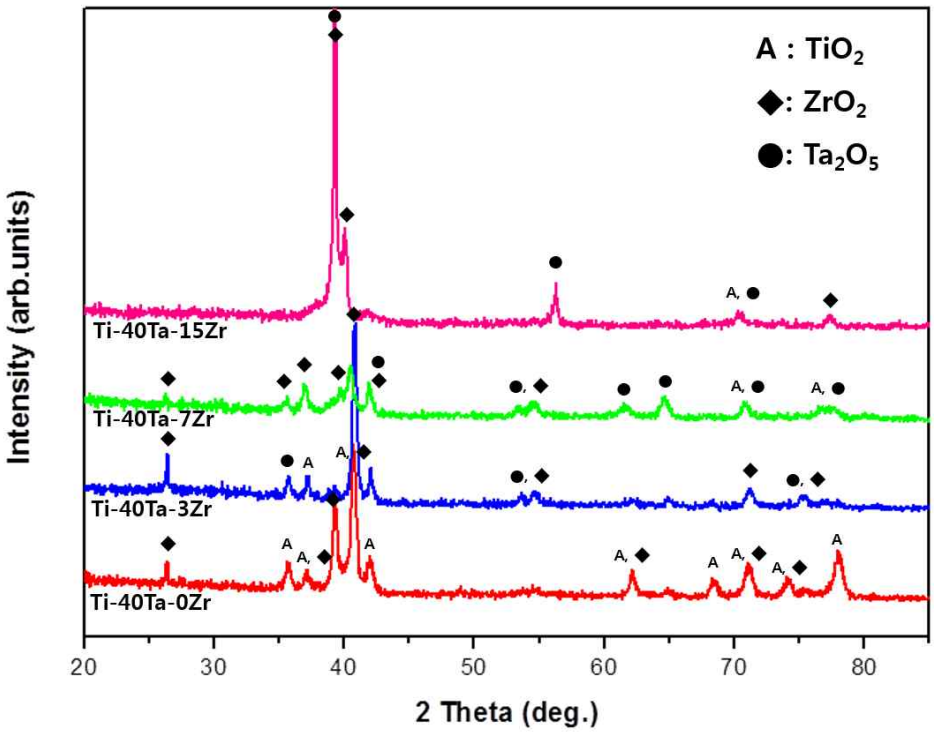


Fig. 13. XRD patterns of PEO-treated Ti-40Ta-xZr alloys in 0.15 M calcium acetate monohydrate + 0.02 M calcium glycerophosphate.

Table 9. Analysis of Ca/P ratio and area occupied by pores on the surface.

| Samples / Properties | Ca / P ratio | [Ca+Mg+Zn] / P ratio | Ratio of area occupied by pore/area of non-occupied by pore (%) | | Distance between pores (㎛) | |
|---|---|---|---|---|---|---|
| | | | Ca and P | Ca, P, Mg, and Zn | Ca and P | Ca, P, Mg, and Zn |
| Ti-40Ta-0Zr | 1.522 | 1.334 | 8.35 | 8.12 | 1.34 | 1.22 |
| Ti-40Ta-3Zr | 1.603 | 1.400 | 9.31 | 9.05 | 1.50 | 1.38 |
| Ti-40Ta-7Zr | 1.678 | 1.535 | 10.18 | 10.17 | 1.96 | 1.80 |
| Ti-40Ta-15Zr | 2.269 | 2.301 | 17.12 | 16.82 | 3.40 | 3.06 |

## Ⅳ. 3. 1. Coating surface analysis of PEO-treated Ti-40Ta-xZr alloys

Fig. 14 and 15 show the EDS results on the PEO-treated Ti-40Ta-xZr alloys in Ca, P, Mg, and Zn electrolyte, respectively. As a result of the EDS analysis, the degree of doping of ions on the surface was found, and the surface Ca / P ratio was obtained.

In Fig. 16, Ca / P ratios were determined on the surface of the alloy on which hydroxyapatite (HA) [$Ca_{10}$ $(PO_4)_6$ $(OH)_2$] was formed by EDS surface analysis (Fig. 14, Fig. 15). Detailed figures are listed in Table 9. Ti-40Ta-7Zr alloy at 1.678 is closest to the ideal Ca / P ratio of 1.667. Also, as the content of added Zr increased, the ratio of Ca / P tended to increase. The same concentration of electrolyte, however, showed that the Ca / P ratio increased with increasing Zr content. This is considered to be the presence of a transition zone consisting of Zr, Ca, O complexes between the exterior and interior of the coating material. Therefore, the $ZrO_2$ phase formed during the PEO process is as follows[33-34].

(1) $Zr \leftrightarrow Zr^{+4} + 4e^-$

(2) $Zr^{+4} + 2O^{-2} \leftrightarrow ZrO_2$

(3) $10\ Ca^{2+} + 6\ PO_4^{3-} + 2\ H_2O \leftrightarrow Ca_{10}\ (PO_4)_6\ (OH)_2 + 2H$

The Zr alloy is used as an anode to form $Zr^{+4}$ ions by losing electrons and react with $O^{2-}$ and $OH^-$ ions present in the electrolyte to form a $ZrO_2$ phase. In addition, when a high-pressure spark of 280 volts occurs on the surface of the coating, calcium and phosphate ions are ionized, the reaction between $Ca^{2+}$, $PO_4^{3-}$ and $H_2O$ occurs on the surface of the alloy, forming $Ca_{10}$ $(PO_4)_6$ $(OH)_2$ and $2H^+$. The $Ca^{2+}$, $Zr^{4+}$, and $OH^-$ ions that react with each other in the high current density and high temperature discharge channels form $CaZrO_3$ in the coating structure. In addition, since the ionic radius of HA (0.99Å) is close to the ionic radius of

$Zr^{4+}$ (0.79Å), $Ca^{2+}$ ions are released from the HA phase and move to the lattice site of $Zr^{4+}$ during $ZrO_2$ oxide formation[35-36]. This is presumed to be due to the increase of Ca / P ratio due to $CaZrO_3$ and HA detected on the coating surface.

The [Ca + Mg + Zn] / P ratio for each specimen was 1.334, 1.4, 1.53, and 2.301. [Ca + Mg + Zn] / P ratio (Fig. 16- b) shows a slight decrease in the ratio compared to the Ca / P ratio. The Ca / P ratio decreases because of the decrease in Ca content. When Mg and Zn ions are added to Ca, P ions, Zn and Mg are pulled into the discharge channel and replaced with Ca sites. Mg ions attracted to the discharge channel act as sites for HA nucleation[14]. The HA chemical equation for the substitution of Ca and Mg ions is as follows:

$$(10-x)Ca^{2+} + xMg^{2+} + 6PO_4^{3-} + 2OH^- \rightarrow Ca_{(10-x)}\ Mg_x\ (PO_4)_6\ (OH)_2\ (0 \leqq x \leqq 10)$$

Also, it is a chemical deformation reaction to replace Ca and Zn ions[16].

(1) $Ca^{2+} + HPO_4^{2-} \rightarrow CaHPO_4$

(2) $3CaHPO_4 \rightarrow Ca_3\ (PO_4)_2 + H_3PO_4$

(3) $3Zn^{2+} + 2H_2PO^{4-} + 2H^+ + 4H_2O + 6e \rightarrow Zn_3\ (PO_4)_2 \cdot 4H_2O + 3H_2\uparrow$

In Fig. 17, Fig. 18, the EDS-mapping analysis of Ti-40Ta-15Zr alloy. Fig. 17 shows PEO treatment in Ca, P electrolyte and Fig. 18 shows PEO treatment in Ca, P, Mg, and Zn electrolyte. The mapping of the elements implanted on the surface of the PEO-treated Ti-40Ta-15Zr alloy is shown. Ti, Ta, and Zn were uniformly distributed, and the other elements showed more tendency to surface than pore interior. This is illustrated in more detail in Fig. 19 and Fig. 20 by analyzing the EDS line profile.

Fig. 19 and 20 show the EDS line profile analysis. Fig. 19 shows Ca, P electrolytes and Fig. 20 shows Ca, P, Mg, and Zn electrolytes. The formation of HA as well as various oxides such as $TiO_2$, $ZrO_2$, $Ta_2O_5$ and $ZnO_2$ can be inferred

from the surface. The atomic radius of the element constituting the oxide is 142 pm for Zn, 155 pm for Zr, 176 pm for Ti, and 200 pm for Ta, and Ta will form the largest atomic radius and will produce stable oxides[37-39]. At the onset of anodic oxidation, Ti, Ta, and Zr elements are separated from the metal to form oxides through the micro-discharge channels and Ca-Zr-O complex oxide[34,40]. HA is expected to form on the upper layer. Substitution of Zn and Mg with Ca is believed to enhance biocompatibility and alleviate bone reactions on the implant surface. The release of Zn from the body is strongly mediated by the osseous reservoir and the addition of Zn to the implant can promote bone formation on the implant surface[41].

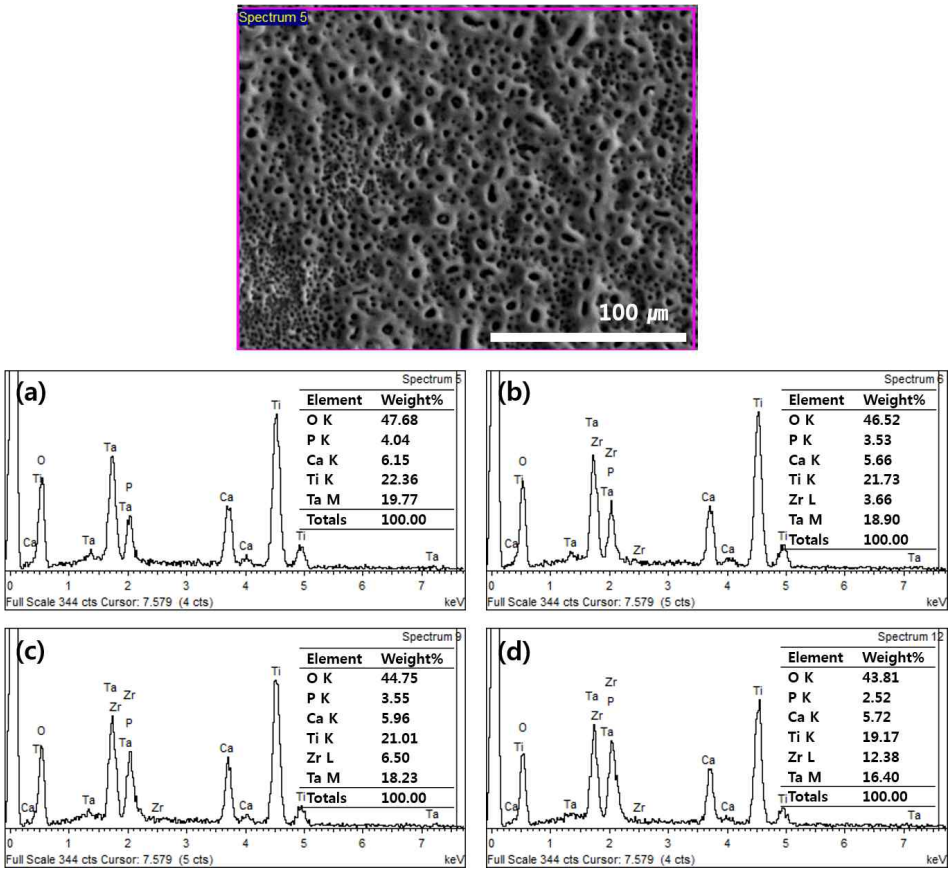


Fig. 14. EDS results of PEO-treated Ti-40Ta-xZr alloys 0.15 M calcium acetate monohydrate + 0.02 M calcium glycerophosphate: (a) Ti-40Ta-0Zr, (b) Ti-40Ta-3Zr, (c) Ti-40Ta-7Zr, and (d) Ti-40Ta-15Zr.

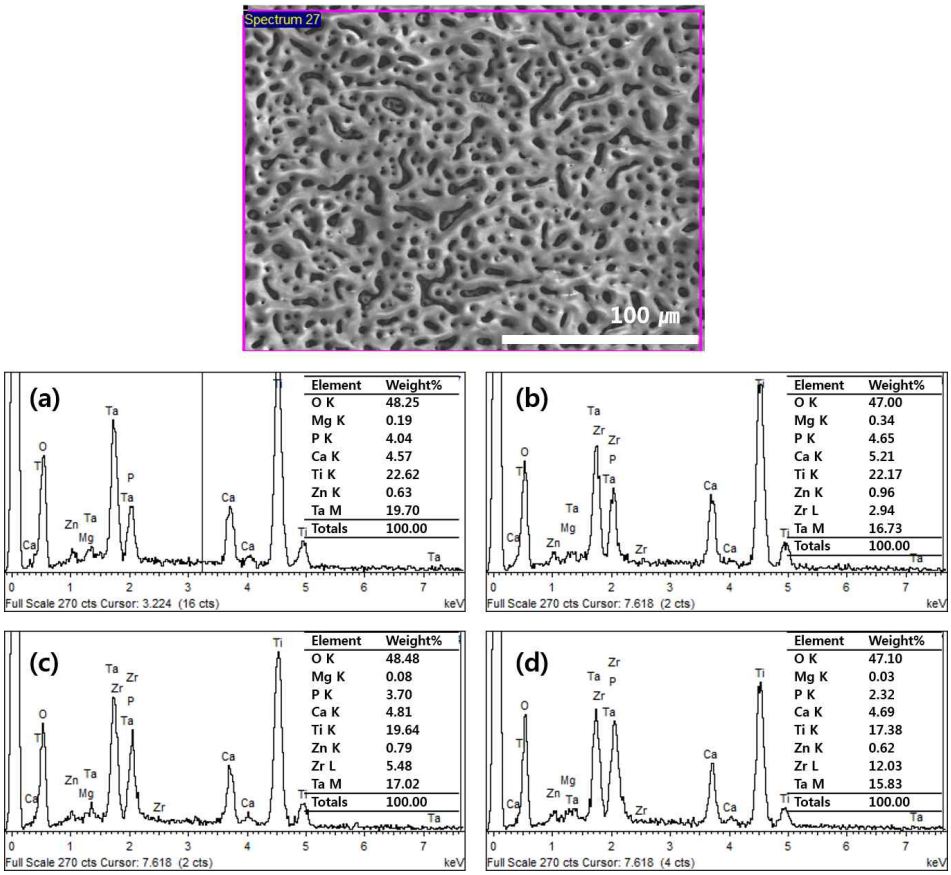


Fig. 15. EDS results of PEO-treated Ti-40Ta-xZr alloys in 0.135 M calcium acetate monohydrate + 0.02 M calcium glycerophosphate + 0.0075 M magnesium acetate tetrahydrate + 0.0075 M zinc acetate dehydrate: (a) Ti-40Ta-0Zr, (b) Ti-40Ta-3Zr, (c) Ti-40Ta-7Zr, and (d) Ti-40Ta-15Zr.

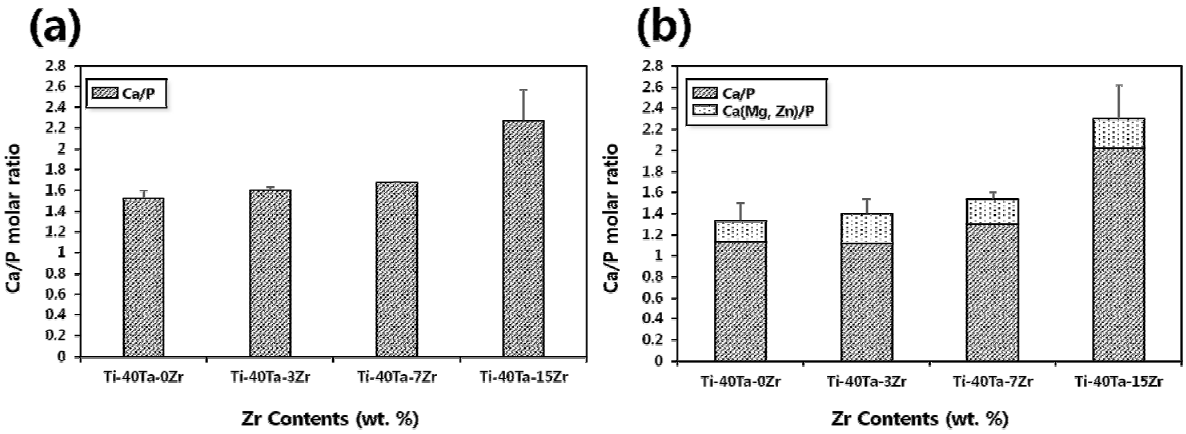


Fig. 16. Ca/P and [Ca+Mg+Zn]/P molar ratio from EDS results: (a) in 0.15 M calcium acetate monohydrate + 0.02 M calcium glycerophosphate, (b) in 0.135 M calcium acetate monohydrate + 0.02 M calcium glycerophosphate + 0.0075 M magnesium acetate tetrahydrate + 0.0075 M zinc acetate dehydrate.

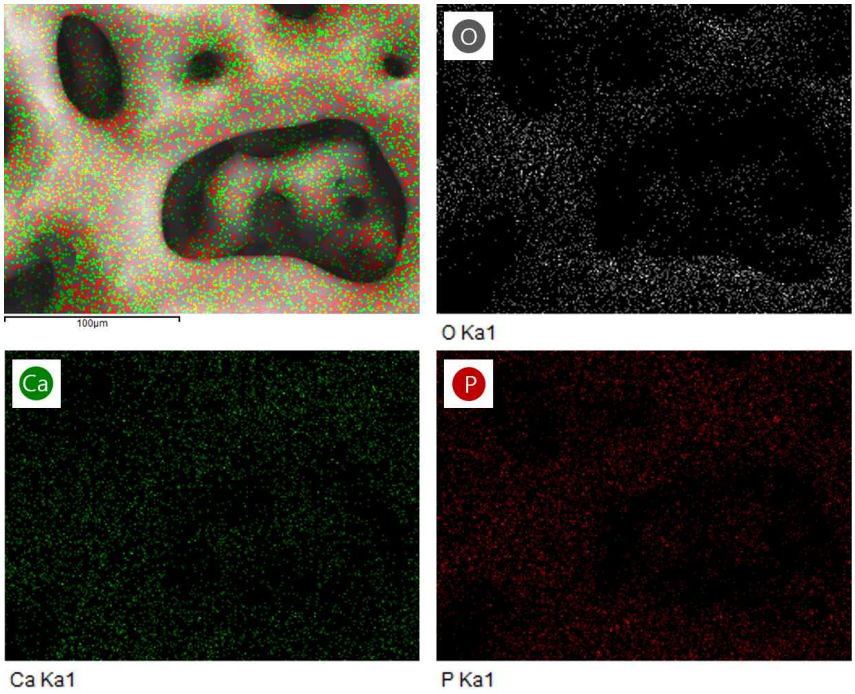


Fig. 17. EDS mapping analysis results of PEO-treated Ti-40Ta-15Zr alloys in 0.15 M calcium acetate monohydrate + 0.02 M calcium glycerophosphate.

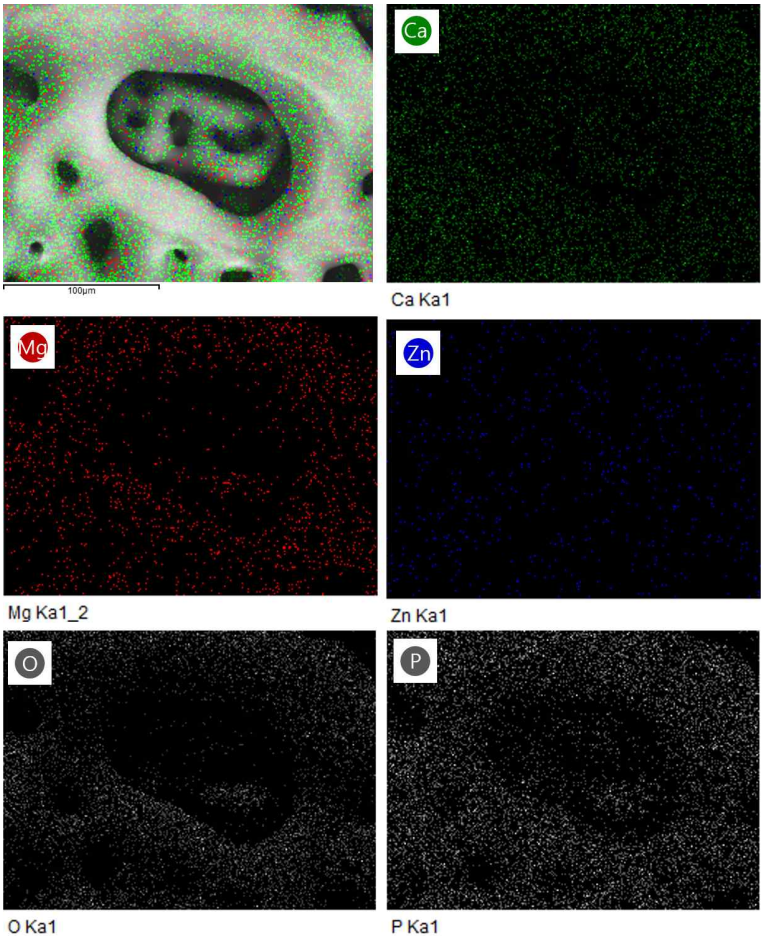


Fig. 18. EDS mapping analysis results of PEO-treated Ti-40Ta-15Zr alloy in 0.135 M calcium acetate monohydrate + 0.02 M calcium glycerophosphate + 0.0075 M magnesium acetate tetrahydrate + 0.0075 M zinc acetate dehydrate.

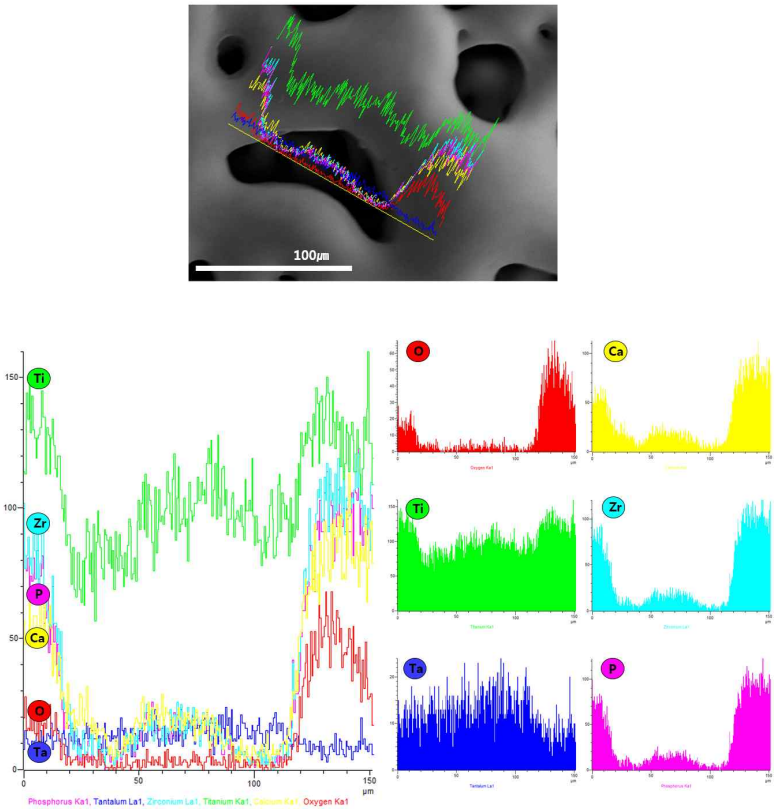


Fig. 19. EDS line-profile analysis results of PEO-treated Ti-40Ta-15Zr alloy in 0.15 M calcium acetate monohydrate + 0.02 M calcium glycerophosphate.

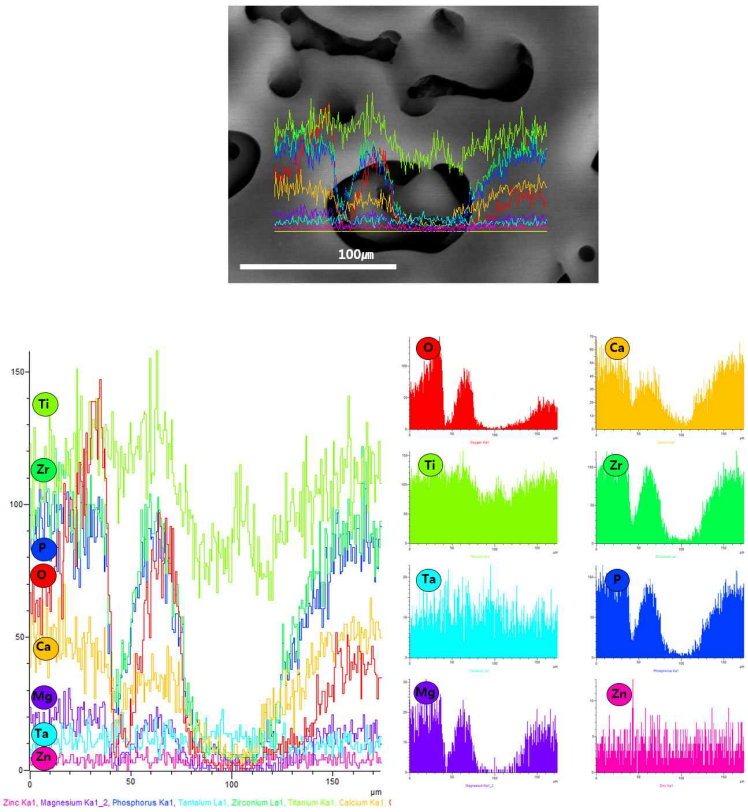


Fig. 20. EDS line-profile analysis results of PEO-treated Ti-40Ta-15Zr alloy in 0.135 M calcium acetate monohydrate + 0.02 M calcium glycerophosphate + 0.0075 M magnesium acetate tetrahydrate + 0.0075 M zinc acetate dehydrate.

## IV. 4. Biocompatibility of Ti-40Ta-xZr alloys

### IV. 4. 1. Effect of alloying elements and surface roughness on the wettability

Fig. 21 shows the contact angle values of Ti-40Ta-xZr alloys with different surface treatment. Fig. 21 (a) to (d) shows contact angle value of non-treated surface, etching surfaces, PEO-treated in Ca, P electrolyte, and PEO-treated in Ca, P, Mg, and Zn electrolyte, respectively. Also, Fig. 22 shows the contact angle of water droplets measured on the different surface treatment. From the result of contact angle test, the contact angle was the highest on the surface without surface modification treatment [Fig. 21(a~a-3)]. The lowest contact angle appeared on the surface where the alloy was etched [Fig. 21(b~b-3)]. Due to the etching process, it is presumed that the lowest contact angle appeared because of needle-like and equiaxed structures on the corroded surface. It is confirmed that surface roughness increases as Zr content decreases due to formation of martensitic structure. This structure shows the rough surface and can be easily corroded by etchant. The PEO-treated surface showed a relatively low contact angle, and a lower contact angle was observed at the surface [Fig. 21(d~d-3)] where Mg and Zn ions were added. In the case of PEO-treated surfaces, contact angle decreased compared to non-PEO treated samples, because of formation of pore on the surface. Also, the change of contact angle showed a little bit increment as Zr content increased. The low contact angle and high surface energy for the PEO-treated Ti-40Ta-xZr alloys are due to the formation of HA on the surface. The HA has been reported to have excellent wettability because of its high surface roughness and high surface energy between alloy and air compared to surface energy between of liquid and alloy surface. Surface free energy plays an important role in affecting metal implants and cell attachment, and is proportional to surface roughness[42].

Fig. 23 and Fig. 24 show the Atomic force microscopy (AFM) analysis of PEO-treated in Ca, P electrolyte, and PEO-treated in Ca, P, Mg, and Zn

electrolyte, respectively. In the case of PEO-treated in solution containing Mg and Zn ions, contact angle decreased compared to bulk and PEO-treated samples in solution containing Ca and P ions. It is consistent that Mg and Zn ions play role to decrease the surface energy between alloy and liquid. The Mg and Zn elements on the PEO-treated surface are expected to promote nonuniform nucleation of apatite micro-particles on the Mg and Zn coated surface and improve biocompatibility by participating in the proliferation and differentiation of osteoblasts[11,43].

From the surface roughness analysis, in the case of PEO-treated in solution containing Ca and P ions, the values of surface roughness($R_a$) [total region (red area)] of samples were 0.181㎛ (a), 0.126㎛ (b), 0.061㎛ (c), and 0.103㎛ (d), respectively, as shown in Fig. 23, as the Zr content increases. In the case of PEO-treated in solution containing Ca, P, Mg, Zn ions, the values of surface roughness($R_a$) [total region (red area)] of samples were 0.374㎛ (a), 0.339㎛ (b), 0.332㎛ (c), and 0.155㎛ (d),respectively, as shown in Fig. 24, as the Zr content increases. Detailed figures are shown in the Table 10.

From the results of AFM, it is confirmed that surface roughness of PEO-treated surface decreased as Zr content increased. Whereas, in the case of PEO-treated surface containing Mg and Zn ions, surface roughness increased. In addition, the surface roughness of PEO-treated surface in solution containing Mg and Zn elements was found to be higher than that of Ca and P electrolytes, which is the influence of the added Mg, Zn elements[14),16),29),42)]. Therefore, it is consistent that contact angles of samples decrease as surface roughness of samples increased.

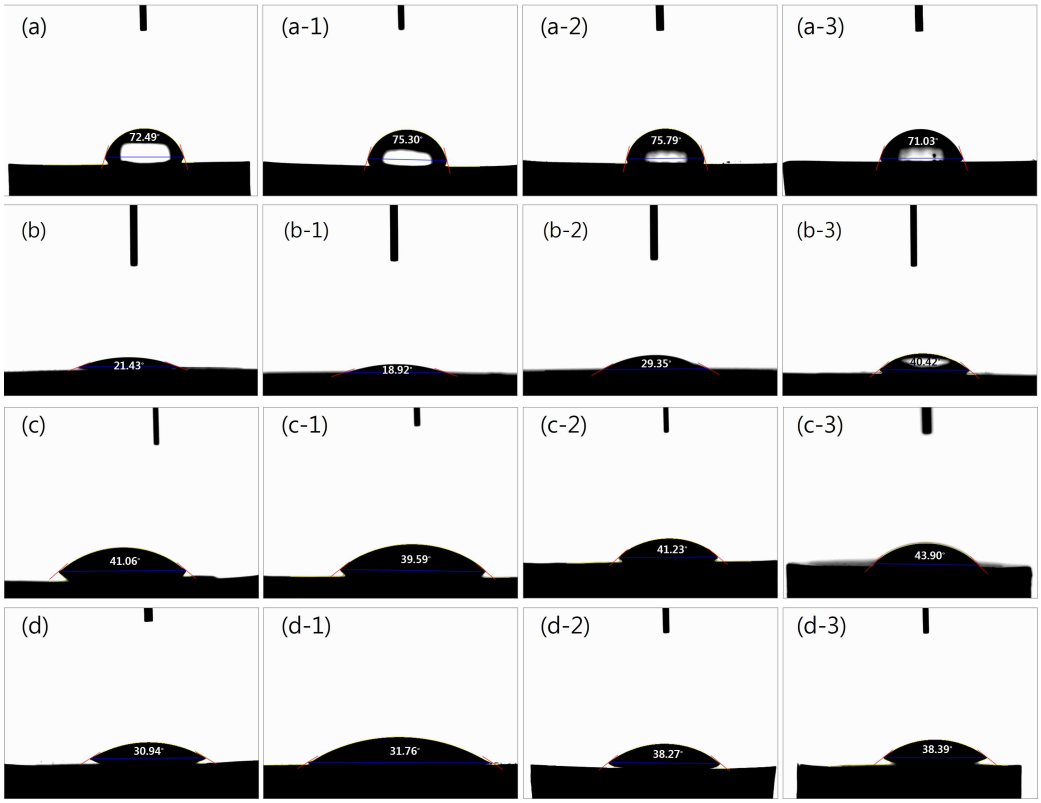


Fig. 21. Contact angles of PEO-treated Ti-40Ta-xZr alloys: (a-d) Ti-40Ta-0Zr, (a-1~d-1) Ti-40Ta-3Zr, (a-2~d-2) Ti-40Ta-7Zr, and (a-3~d-3) Ti-40Ta-15Zr:

(a)~(a-3): non-treated,

(b)~(b-3): Etched surface,

(c)~(c-3): Electrolyte in 0.15 M calcium acetate monohydrate + 0.02 M calcium glycerophosphate,

(d)~(d-3): Electrolyte in 0.135 M calcium acetate monohydrate + 0.02 M calcium glycerophosphate + 0.0075 M magnesium acetate tetrahydrate + 0.0075 M zinc acetate dehydrate.

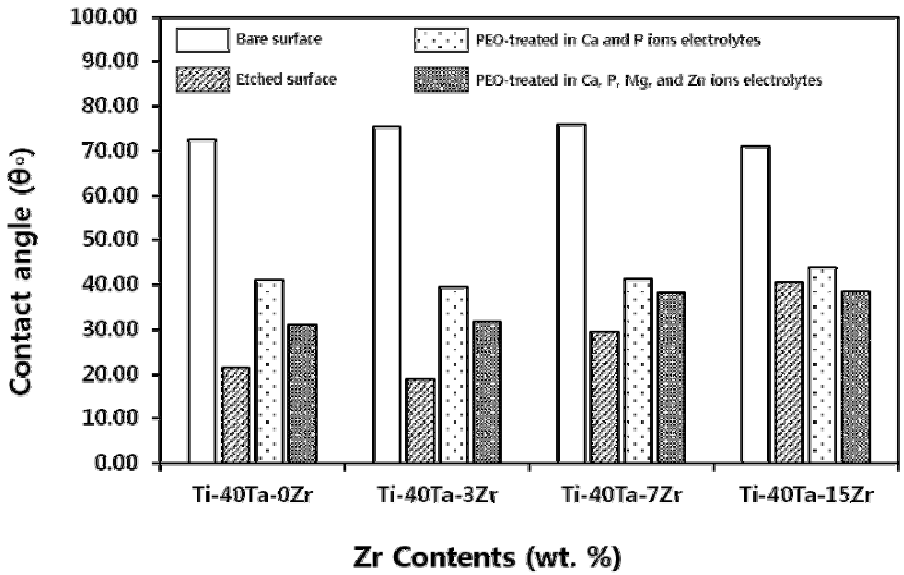


Fig. 22. Contact angles of water droplets measured on the different surface treatment.

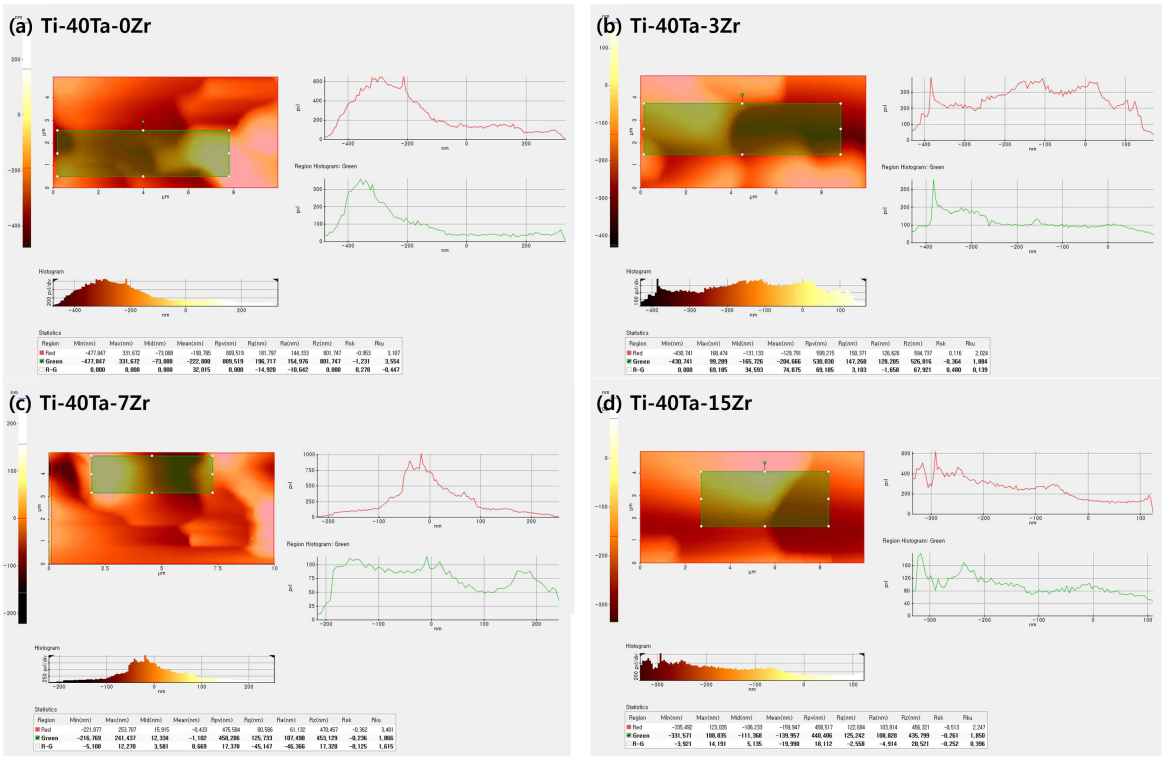


Fig. 23. Surface roughness of PEO-treated Ti-40Ta-15Zr alloy in 0.15 M calcium acetate monohydrate + 0.02 M calcium glycerophosphate by AFM analysis: (a) Ti-40Ta-0Zr, (b) Ti-40Ta-3Zr, (c) Ti-40Ta-7Zr, and (d) Ti-40Ta-15Zr.

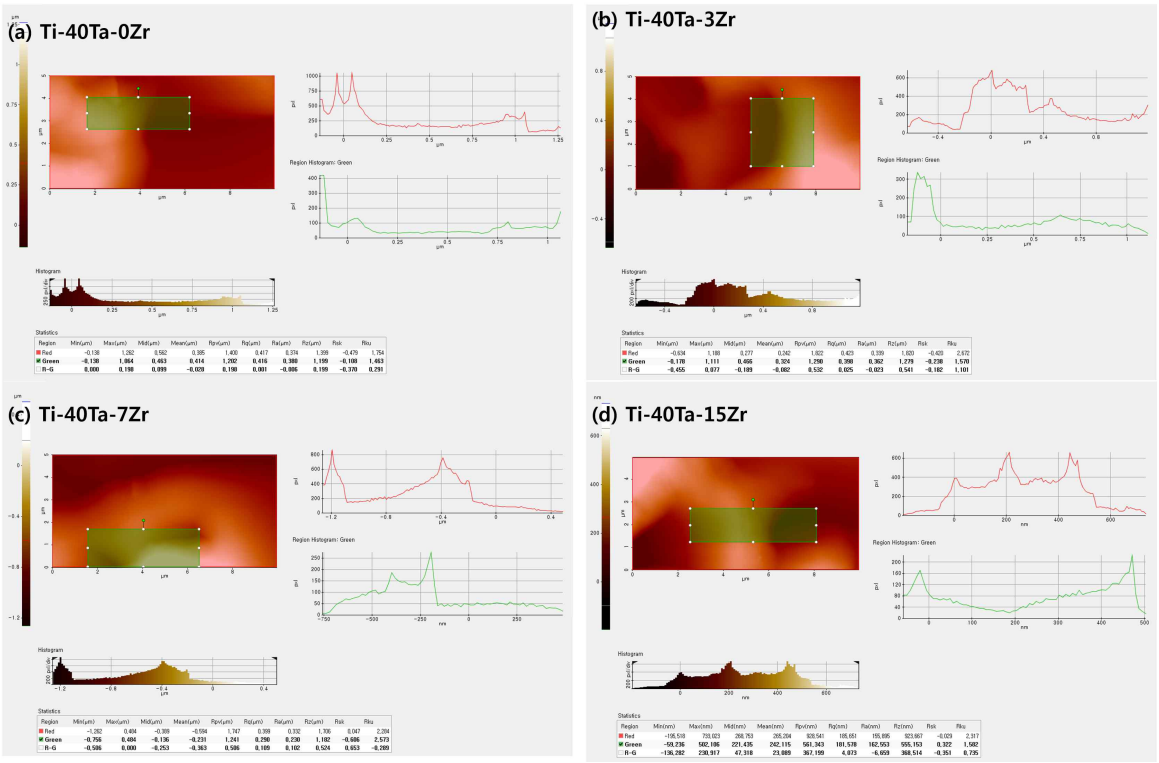


Fig. 24. Surface roughness of PEO-treated Ti-40Ta-15Zr alloy in 0.135 M calcium acetate monohydrate + 0.02 M calcium glycerophosphate + 0.0075 M magnesium acetate tetrahydrate + 0.0075 M zinc acetate dehydrate by AFM analysis: (a) Ti-40Ta-0Zr, (b) Ti-40Ta-3Zr, (c) Ti-40Ta-7Zr, and (d) Ti-40Ta-15Zr.

Table 10. Surface roughness of PEO-treated Ti-40Ta-xZr alloys.

| Samples / Properties | Ca and P electrolyte (㎛) | Ca, P, Mg, and Zn electrolyte (㎛) |
|---|---|---|
| Ti-40Ta-0Zr | 0.181 | 0.374 |
| Ti-40Ta-3Zr | 0.126 | 0.339 |
| Ti-40Ta-7Zr | 0.061 | 0.332 |
| Ti-40Ta-15Zr | 0.103 | 0.155 |

## Ⅳ. 4. 2. Cell culture on the PEO-treated Ti-40Ta-xZr alloys

Fig. 23 and 24 show the FE-SEM micrographs images showing HEK 293 (Human embryonic kidney 293) cell cultured on the Ti-40Ta-xZr alloysat 37 ℃ for 24 h with various surface treatment. As the control group, Ti-40Ta-xZr alloys treated with PEO in Ca, P electrolyte was used (Fig. 23), in the experimental group, PEO-treated Ti-40Ta-xZr alloys were used for Ca, P, Mg, and Zn electrolytes (Fig. 24). As a result, in the control and experimental group, cell proliferation and differentiation were good. The pores and surfaces were well covered with lamellipodia and filopodia on the PEO-treated Ti-40Ta-7Zr and Ti-40Ta-15Zr alloys in the solution containing Ca, P, Mg, and Zn ions.

Therefore, the influence of Mg and Zn elements doped on the alloy surface in the PEO process was larger than that of non-doped alloy. Previous studies have shown that Zn-injected titanium has a partially antibacterial effect on both E. coli and Staphylococcus aureus and stimulates osteoblast proliferation, early attachment and spreading. Mg is the most abundant cation in the human body and these are cofactors for many enzymes that induce osteoblast proliferation. Therefore, magnesium plays an active role in the process of new bone tissue formation process[40-47].

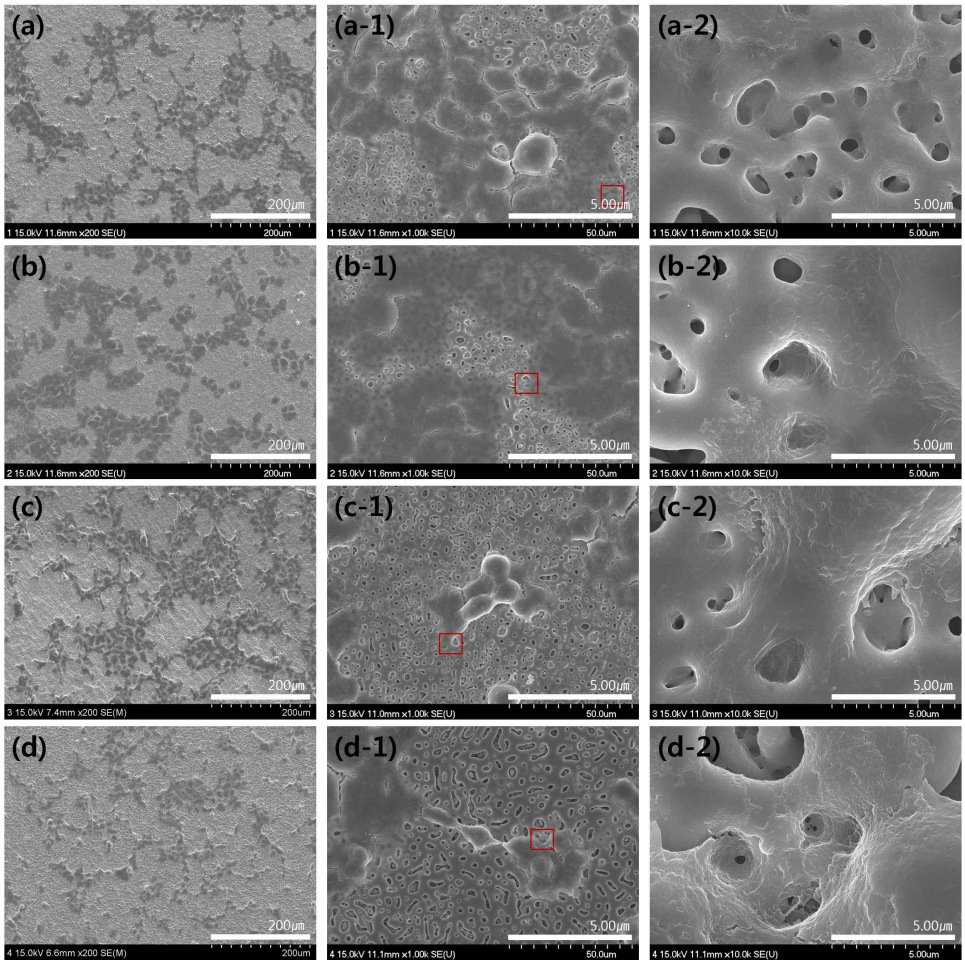


Fig. 25. FE-SEM images of HEK 293 cell cultured on Ti-40Ta-xZr alloys in 0.15 M calcium acetate monohydrate + 0.02 M calcium glycerophosphate: (a~a-2) Ti-40Ta-0Zr, (b~b-2) Ti-40Ta-3Zr, (c~c-2) Ti-40Ta-7Zr, and (d~d-2) Ti-40Ta-15Zr.

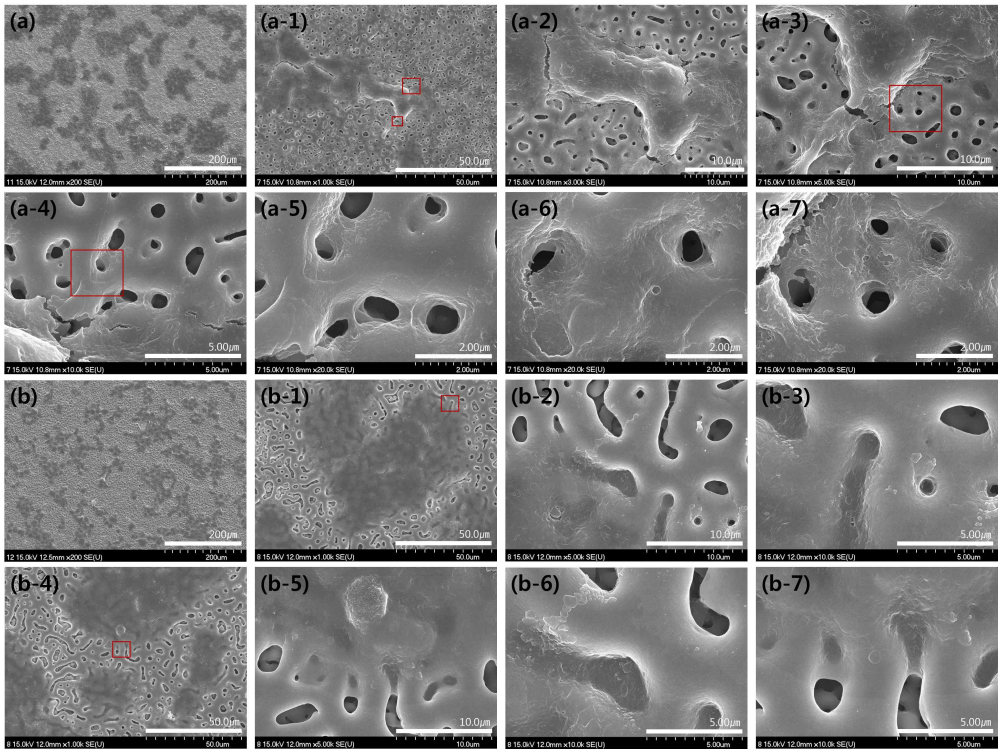


Fig. 26. FE-SEM images of HEK 293 cell cultured on Ti-40Ta-xZr alloys in 0.135 M calcium acetate monohydrate + 0.02 M calcium glycerophosphate + 0.0075 M magnesium acetate tetrahydrate + 0.0075 M zinc acetate dehydrate: (a~a-7) Ti-40Ta-7Zr, and (b~d-7) Ti-40Ta-15Zr.

# Ⅴ. CONCLUSIONS

In this study, surface characteristics and biocompatibility of PEO-treated Ti-40Ta-xZr alloy in electrolytes containing Ca, P, Mg, and Zn ions have been researched. The results were as follows;

1. In the microstructure of the Ti-40Ta-xZr alloys, both α and β phase were appeared. As the Zr content increased, the shape of the needle-like decreased and the shape of the equiaxed structure and the β phase increased.

2. As the Zr content increases in the Ti-40Ta-xZr alloy, the elastic modulus and vickers hardness values tend to decrease. When Zr is added to Ta, the α phase gradually disappears, whereas, the β phase appears, the elastic modulus decreases and vickers hardness decreases, simultaneously.

3. Porosity was formed on the PEO-treated surface, and as the Zr content increased, the pore size was increased and secondary pore was formed in the first formed pore. From the result of AFM, the surface roughness decreased with increasing Zr content. In the PEO process, oxides such as $TiO_2$, $Ta_2O_5$, and $ZrO_2$ were formed on the alloy surface through micro-discharge channels.

4. The Ca / P ratio was the closest to the ideal value for Ti-40Ta-7Zr, and after addition of Mg and Zn ions, the Ca / P ratio decreased as Mg and Zn were replaced with Ca site.

5. From the results of EDS analysis, Ti, Ta, and Zn were uniformly distributed, and the other elements showed more tendency to surface than pore interior. The formation of HA as well as various oxides such as $TiO_2$,

$ZrO_2$, $Ta_2O_5$, and $ZnO_2$ can be inferred from the surface.

6. The low contact angle and high surface energy for the PEO-treated Ti-40Ta-xZr alloys and cell proliferation and differentiation were good in the PEO-treated Ti-40Ta-7Zr and Ti-40Ta-15Zr alloys in Ca, P, Mg and Zn electrolytes with lamellipodia and filopodia covered the pores and surfaces.

# - Reference -

1. M. Niinomi, M. Nakai, J. Hieda, Development of new metallic alloys for biomedical applications, Acta Biomater. 8 (2012) 3888.
2. H. C. Choe, W. G. Kim, Y. H. Jeong, Surface characteristics of HA coated Ti-30Ta-xZr and Ti-30Nb-xZr alloys after nanotube formation, Surf. Coat. Technol. 205 (2010) 305.
3. H. J. Kim, Y. H. Jeong, H. C, Choe, W. A. Brentley, Hydroxyapatite formation on biomedical Ti-Ta-Zr alloys by magnetron sputtering and electrochemical deposition, Thin Solid Films 572 (2014) 119.
4. J. J. Kim, I.S. Byeon, W. A. Brantley, H. C. Choe, Highly ordered nanotubular film formation on Ti-25Nb-xZr and Ti-25Ta-xHf, Thin Solid Films 596 (2015) 94.
5. J. Izquierdo, G. Bolat, N. Cimpoesu, L. C. Trinca, D. Mareci, R. M. Souto, Electrochemical characterization of pulsed layer deposited hydroxyapatite-zirconia layers on Ti-21Nb-15Ta-6Zr alloy for biomedical application, Appl. Surf. Sci. 385 (2016) 368.
6. S. L. Aktug, I. Kutbay, M. Usta, Characterization and formation of bioactive hydroxyapatite coating on commercially pure zirconium by micro arc oxidation, J. Alloy. Compd. 695 (2017) 998.
7. W. G. Kim, H. C. Choe, W. A. Brantley, Nanostructured surface changes of Ti-35Ta-xZr alloys with changes in anodization factors, Thin Solid Films 519 (2011) 4663.
8. S. Durdu, O. F. Deniz, I. Kutbay, M. Usta, Characterization and formation of hydroxyapatite on Ti6Al4V coated by plasma electrolytic oxidation, J. Alloys Compd. 551 (2013) 422.
9. C. Capuccini, P. Torricelli, F. Sima, E. Boanini, C. Ristoscu, B. Bracci, G. Socol, M. Fini, I.N. Mihailescu, A. Bigi, Strontium-substituted hydroxyapatite coatings synthesized by pulsed-laser deposition: In vitro osteoblast and osteoclast response, Acta Biomater. 4 (2008) 1885.
10. K. Lee, H.C. Choe, Effects of electrolyte concentration on formation of

calcium phosphate films on Ti-6Al-4V by electrochemical deposition, J. Nanosci. Nanotechnol. 17 (2017) 2743.

11. E. Boanini, M. Gazzano, A. Bigi, Ionic substitutions in calcium phosphates synthesized at low temperature, Acta Biomater. 6 (2010) 1882.
12. V. Aina, L. Bergandi, G. Lusvardi, G. Malavasi, F. E. Imrie, I. R. Gibson, G. Cerrato, D. Ghigo, Sr-containing hydroxyapatite: morphologies of HA crystals and bioactivity on osteoblast cells, Mater Sci Eng C 33 (2013) 1132.
13. S. C. Cox, P. Jamshidi, L. M. Grover, K. K. Mallick, Preparation and characterisation of nanophase Sr, Mg, and Zn substituted hydroxyapatite by aqueous precipitation, Mater. Sci. Eng. C 35 (2014) 106.
14. J. M. Yu, H. C. Choe, Mg-containing hydroxyapatite coatings on Ti-6Al-4V alloy for dental materials, Appl. Surf. Sci. 432 (2018) 294.
15. T. Huang, Y. Xiao, S. Wang, Y. Huang, X.Liu, F. Wu, Z. Gu, Nanostructured Si, Mg, $CO_3^{2-}$ Substituted Hydroxyapatite Coatings Deposited by Liquid Precursor Plasma Spraying: Synthesis and Characterization, J. Therm. Spray Technol. 20 (2011) 829.
16. I. J. Hwang, H. C. Choe, Effects of Zn and Si ions on the corrosion behaviors of PEO-treated Ti-6Al-4V alloy, Appl. Surf. Sci. https://doi.org/10.1016/j.apsusc.2017.12.015
17. Y. Okazaki, Y. Ito, A. Ito, T. Tateishi, Effect of Alloying Elements on Mechanical Properties of Titanium Alloys for Medical Implant, Mater Trans Jim 34 (1993) 1217.
18. X. Liu, P. K. Chu, C. Ding, Surface modification of titanium, titanium alloys, and related materials for biomedical applications, Mater. Sci. Eng. R 47 (2004) 49.
19. M. Niinomi, D. Kuroda, K. I. Fukunaga, M. Morinaga, Y. Kato, T. Yashiro, A. Suzuki, Corrosion wear fracture of new β type biomedical titanium alloys , Mater. Sci. Eng. A 263 (1999) 193.
20. I. J. Hwang, H. C. Choe, Hydroxyapatite coatings containing Zn and Si on

Ti-6Al-4Valloy by plasma electrolytic oxidation, Appl. Surf. Sci. 432 (2018) 337.

21. I. J. Hwang, H. C. Choe, W. A. Brantley, Electrochemical characteristics of Ti-6Al-4V after plasma electrolytic oxidation in solutions containing Ca, P, and Zn ions, Surf. Coat. Technol. 320 (2017) 458.

22. S. Durdu, O. F. Deniz, I. Kutbay, M. Usta, Characterization and formation of hydroxyapatite on Ti6Al4V coated by plasma electrolytic oxidation, J. Alloys Compd. 551 (2013) 422.

23. R. O. Hussein, X. Nie, D. O. Northwood, An investigation of ceramic coating growth mechanisms in plasma electrolytic oxidation (PEO) processing, Electrochimica Acta 112 (2013) 111.

24. Y. L. Zhou, M. Niinomi, T. Akahori, Effects of Ta content on Young's modulus and tensile properties of binary Ti-Ta alloys for biomedical applications, Mater. Sci. Eng. A 371 (2004) 283.

25. Y. L. Zhou, M. Niinomi, T. Akahori, M. Nakai, H. Fukui, Comparison of Various Properties between Titaniunm-Tantalum Alloy and Pure Titanium for Biomedical Applications, Materials Transactions 48 (2007) 380.

26. J. Zhao, X. Wang, R. Chen, L. Li, Fabrication of titanium oxide nanotube arrays by anodic oxidation, Solid State Commun. 134 (2005) 705.

27. A. V. Dobromyslove, V. A. Elkin, Martensitic transformation and metastable β-phase in binary titanium alloys with d-metals of 4-6 periods, Scripta Mater. 44 (2001) 905.

28. A. L. R. Riveiro, R. C. Junior, F. F. Cardoso, R. B. F. Filho, L. G. Vaz, Mechanical, physical, and chemical characterization of Ti-35Nb-5Zr and Ti-35Nb-10Zr casting alloys, J. Mater. Sci: Mater. Med. 20 (2009) 1629.

29. X. Yang, S. Yu, Wen. Li, Preparation of bioceramic films containing hydroxyapatites on Ti-6Al-4V alloy surfaces by the micro-arc oxidation technique, Mater. Res. Bull. 44 (2009), 947.

30. A. L. Yerokhin, V. V. Lyubimov, R. V. Ashitkv, Phase formation in

ceramic coatings during plasma elemctrolytic oxidation of aluminium alloys, Ceram. Int. 24 (1998) 1.

31. J. M. Yu, H. C. Choe, Morphology Changes of Plasma Electrolytic Oxidized Ti-6Al-4V Alloy in the Electrolytes Containing Sr and Si Ions, Journal of Nanoscience and Nanotechnology 18 (2018) 833.

32. J. M. Yu, H. C. Choe, Morphology change and bone formation on PEO-treated Ti-6Al-4V alloy in electrolyte containing Ca, P, Sr, and Si ions, Appl. Surf. Sci. (2017) https://doi.org/10.1016/j.apsusc.2017.11.223

33. S. L. Aktuğ, S. Durdu, E. Yalç ı n, K. Çavuşoğlu, M. Usta, Bioactivity and biocompatibility of hydroxyapatite-based bioceramic coatings on zirconium by plasma electrolytic oxidation, Mater. Sci. Eng. C 71 (2017) 1020.

34. S. Cengiz, A. Uzunoglu, L. Stanciu, M. Tarakci, Y. Gencer, Direct fabrication of crystalline hydroxyapatite coating on zirconium bysingle-step plasma electrolytic oxidation process, Surf. Coat. Technol. 301 (2016) 74.

35. S. L. Aktug, I. Kutbay, M. Usta, Characterization and formation of bioactive hydroxyapatite coating on commercially pure zirconium by micro arc oxidation, J. Alloys Compd. 695 (2017) 998.

36. M. Sandhyarani, N. Rameshbabu, K. Venkateswarlu, L. Rama Krishna, Fabrication, characterization and in-vitro evaluation of nanostructured zirconia/hydroxyapatite composite film on zirconium, Surf. Coat. Technol. 238 (2014) 58.

37. A. Kilic, E. Shim, B. Y. Yeom, B. Pourdeyhimi, Improving electret properties of PP filaments with barium titanate, J. Electrost. 71 (2013) 41.

38. Y. Wang, Y. Shen, Z. Zhou, Structures and elastic properties of paraelectric and ferroelectric $KTa_{0.5}Nb_{0.5}O_3$ from first-principles calculation, Physica B 406 (2011) 850.

39. W. Yang, H. Liu, Q. Wang, Z. Wei, L. Xue, C. Dun, Y. Zhao, C. Chang, B.

Shen, Electronic structure of $Cu100-_xZr_x$ (x = 40, 50, 60) metallic glasses, Mater. Design 82 (2015) 126.

40. W. Xue, Q. Zhu, Q. Jin, M. Hua, Characterization of ceramic coatings fabricated on zirconium alloy by plasma electrolytic oxidation in silicate electrolyte, Mater. Chem. Phys. 120 (2010) 656.

41. Y. Tang, H. F. Chappell, M. T. Dove, R. J. Reeder, Y. J. Lee, Zinc incorporation into hydroxyapatite, Biomaterials 30 (2009) 2864.

42. S. L. Aktuğ, S. Durdu, E. Yalç ın, K. Çavuşoğlu, M. Usta, In vitro properties of bioceramic coatings produced on zirconium by plasma electrolytic oxidation, Surf. Coat. Technol. 334 (2017) 129.

43. F. Rupp, L. Liang, J. F. Ferstrfer, L. Scheideler, F. Huttig, Surface characteristics of dental implants: A review, Dental Materials 34 (2018) 40.

44. G. Jin, H. Cao, Y. Qiao, F. Meng, H. Zhu, X. Liu, Osteogenic activity and antibacterial effect of zinc ion implanted titanium, Colloid Surf B 117 (2014) 158.

45. H. Hu, W. Zhang, Y. Qiao, X. Jiang, X. Liu, C. Ding, Antibacterial activity and increased bone marrow stem cell functions of Zn-incorporated $TiO_2$ coatings on titanium, Acta. Biomaterialia 8 (2012) 904.

46. S. Onder, F. N. Kok, K. Kazmanli, M. Urgen, Magnesium substituted hydroxyapatite formation on (Ti,Mg)N coatings produced by cathodic arc PVD technique, Mater Sci Eng C. 33 (2013) 4337.

47. P. J. P. Espitia, J. S. R. Coimbra, R. S. Cruz, E. A. A. Mediros, Zinc oxide nanoparticles: sysntesis, antimicrobial activity and food packging applications, Food Bioprocess Technol. 5 (2012) 1447.